machines

MDPI

Article

Flow-Field Modeling and Mixing Mechanisms of the Twin-Shaft Mixers Based on LBM–LES Coupling

Wentao Zhao [1], Jianxiong Ye [1,*], Lin Li [2] and Gaoan Zheng [3]

[1] School of Intelligent Transportation, Zhejiang Polytechnic University of Mechanical and Electrical Engineering, Hangzhou 310053, China; zhaowentao@zime.edu.cn
[2] College of Mechanical Engineering, Zhejiang University of Technology, Hangzhou 310014, China; linli@zjut.edu.cn
[3] School of Mechanical Engineering, Zhejiang University of Water Resources and Electric Power, Hangzhou 310018, China; zhengga@zjweu.edu.cn
* Correspondence: yejianxiong@zime.edu.cn

Abstract

In modern industrial systems, twin-shaft mixers are key units for efficient mixing and reactions; their performance directly affects product quality, production cycle, and energy consumption across the chemical, pharmaceutical, food, and lithium-battery-slurry sectors. Systematic elucidation of the mixing mechanisms is hindered by strongly three-dimensional, unsteady, and nonlinear flow fields induced by the complex motions of the two shafts. To address these issues, an advanced coupled numerical model combining the lattice Boltzmann method (LBM) and large-eddy simulation (LES) in an integrated LBM–LES framework is developed, incorporating the Smagorinsky subgrid-scale model to capture small-scale turbulent dissipation under high-Reynolds-number conditions with fidelity. The model enables systematic simulations across configurations with varying blade counts, quantitatively revealing how blade count governs flow structures and mixing performance. The results show that blade count is a key design parameter for performance tuning. A four-blade configuration generates moderately strong, well-distributed turbulence and vortical structures in both the main-shaft and side-shaft regions. The generated turbulence and vortical structures, in turn, promote effective global blending and mass transfer while avoiding localized energy over concentration, unnecessary power loss, and overheating risk, thereby achieving an optimal balance among mixing efficiency, energy consumption, and operational stability. These findings provide a solid theoretical basis and a reliable numerical paradigm for the refined design and performance optimization of industrial mixing equipment.

Keywords: twin-shaft mixer; LBM–LES coupling; dynamical modeling; blade count; mixing mechanism

Check for updates

Academic Editor: Davide Lengani

Received: 14 October 2025
Revised: 14 November 2025
Accepted: 21 November 2025
Published: 1 January 2026

Copyright: © 2026 by the authors. Licensee MDPI, Basel, Switzerland. This article is an open access article distributed under the terms and conditions of the Creative Commons Attribution (CC BY) license.

1. Introduction

With the continuing shift in modern industrial technology toward high precision and integration, mixing equipment—as a key process unit—has seen increasingly widespread use in chemical, pharmaceutical, food, lithium-battery slurry, and advanced-materials industries. In complex processes involving non-Newtonian fluids, high-viscosity media, and multiphase mixing, twin- and even multi-shaft mixers have become core equipment for efficient mass transfer, uniform mixing, and reaction intensification owing to their

pronounced advantages in shaping flow fields and enhancing mixing efficiency. By combining impeller types and coordinating their motions, such devices establish complex yet organized flow structures within the vessel, thereby improving mixing quality, augmenting heat and mass transfer, and ultimately exerting decisive influence on product consistency, production cycle, and energy consumption [1–4]. Accordingly, in-depth investigation of the unsteady, strongly nonlinear fluid dynamics inside twin-shaft mixers and systematic elucidation of their mixing mechanisms are crucial for structural optimization, precise tuning of operating parameters, implementation of process-intensification strategies, and improvements in energy efficiency. Dissecting the multiscale physics from macroscopic flow fields to microscopic mixing in stirred tanks provides a solid scientific basis and engineering support for developing the next generation of energy-efficient mixers and advancing industrial technology. During mixing-driven mass transfer, vigorous dynamic interactions among the fluid, rapidly rotating blades, and stationary vessel walls generate highly complex three-dimensional, unsteady flow structures spanning laminar, transitional, and fully turbulent regimes. These jointly govern momentum transport and energy dissipation and thus profoundly determine the spatiotemporal distribution of the flow at both macro- and microscales [5–8]. Although conventional experiments can supply key validation data for specific conditions, their use is often constrained by cost and time and by limits in spatiotemporal resolution, making it difficult to capture the global details of transient unsteady structures such as the generation, evolution, and shedding of tip vortices [9–12]. Computational fluid dynamics (CFD), with its unique advantages of full-field access, multiparameter control, and visualization, has become an indispensable modern tool for resolving complex in-mixer flow mechanisms. By building high-fidelity multiphysics models, the CFD can effectively simulate and reveal the intrinsic links between flow structures and mixing efficiency, offering a robust theoretical basis and numerical testbed for performance prediction and structural innovation of mixing equipment.

Nevertheless, numerical computation of mixer flow fields still faces multiple scientific and technical challenges. The primary difficulty lies in accurately characterizing the highly nonlinear and unsteady turbulent motions that arise during mixing. Under high Reynolds numbers, the flow exhibits pronounced anisotropy and an energy cascade, which directly governs mixing efficiency, the distribution of energy dissipation, and heat- and mass-transfer performance. Moreover, many mixing operations are markedly exothermic or endothermic. Such strong two-way thermo-fluid coupling not only intensifies the nonlinearity of the governing equations but also imposes stringent demands on the stability of numerical schemes and on computational resources. Such strong two-way thermo-fluid coupling not only intensifies the nonlinearity of the governing equations but also imposes stringent demands on the stability of numerical schemes and on computational resources. In response to these key issues, extensive studies have been conducted worldwide. Wang et al. investigated the hydrodynamics and mixing characteristics of non-Newtonian fluids in a dual-shaft eccentric mixer. They showed that counter-rotation and increased eccentricity can markedly shorten the mixing time, and they emphasized that appropriate impeller combinations and spatial arrangements are critical to enhancing overall mixing performance [13]. Li et al. employed a dynamic sliding multi-region approach to simulate the effects of eccentricity on the internal flow of a mixed-flow pump. Eccentricity was found to induce pronounced distortion in the circumferential pressure distribution at both inlet and outlet, thereby reducing head and efficiency at the design condition, whereas the mid-span region of the impeller was relatively less affected by rotational effects [14]. Using CFD, Talhaoui et al. compared fluid mixing behaviors across several improved mixer configurations and identified the helical-overlap mixing elements and diameter aspect ratio as parameters with a substantial impact on mixing efficiency. The optimized design

outperformed the conventional Kenics mixer in both mixing rate and uniformity [15]. Woziwodzki et al. examined anomalous mixing with twin-turbine impellers under laminar conditions and found that increasing impeller eccentricity modifies and shrinks isolated mixing regions, whose morphology depends strongly on the dimensionless eccentricity [16]. From experiments on various configurations of a dual-shaft PBI mixer in a standard baffled tank, Raval et al. observed periodic impeller trajectories at low speeds and chaotic motion at high speeds. The RMS displacement increased exponentially with rotation speed and further increased with dual-impeller operation. With increasing speed, spectral energy in the trajectories shifted from second harmonics to synchronous and sub-synchronous bands, while phase relations and vortex directions were jointly regulated by speed and inter-impeller spacing [17]. Bobba et al. used the discrete element method to simulate size segregation and densification of metal powders when a dual-shaft mixer fills an axisymmetric mold with stepped inner walls under vertical vibration. They found that large amplitudes tend to drive coarse particles to aggregate near the central bottom of the mold, whereas high-frequency vibration and phase differences can trigger surface waves in the stepped regions, affecting distribution uniformity and compaction quality [18]. Trad et al. assessed how impeller design and operating parameters affect distributed mixing in dual-impeller anaerobic digesters; they identified the lower impeller geometry as the dominant factor for macroscopic mixing time and proposed a new dual-impeller configuration that markedly improves mixing efficiency at low energy input by strengthening axial circulation [19]. Emmerink et al. combined the discrete element method with a Plackett–Burman experimental design to quantify the effects of material properties, operating conditions, and geometric parameters on mixing performance in dual-shaft batch paddle mixers. They found that geometry strongly influences energy consumption but has a comparatively minor effect on mixing quality and time, and they further revealed an intrinsic linkage between the particle "temperature" in the blade-center region and the mixing time [20].

A review of existing studies indicates that research on twin-shaft mixing systems has concentrated mainly on macroscopic metrics—such as mixing time, hydraulic losses, and power consumption. In contrast, fine-grained analyses of the transient flow structures and mixing mechanisms driven by the complex dual-shaft motions remain insufficient. Despite substantial advances in conventional computational fluid dynamics (CFD), inherent limitations continue to constrain the depth of related investigations. For example, when dealing with complex moving boundaries such as dual-shaft rotation, sliding-mesh and overset-mesh techniques often incur high computational overheads and potential accuracy losses due to frequent mesh updates and data interpolation. Meanwhile, widely used Reynolds-averaged approaches are intrinsically time-averaged models and therefore struggle to resolve the key transient phenomena that govern mixing efficiency, including vortex shedding, breakup, and material entrainment. Owing to the intrinsic asymmetry and strong unsteady interactions in twin-shaft systems, the underlying flow physics are substantially more complex than in single-shaft counterparts, and systematic studies that elucidate the internal linkage between such dynamic behaviors and overall mixing efficiency remain limited.

This study formulates a coupled lattice Boltzmann–large-eddy simulation (LBM–LES) framework to investigate the hydrodynamics and mixing mechanisms of twin-shaft mixers. The framework incorporates the Smagorinsky subgrid-scale model to represent small-scale turbulent dissipation, thereby providing a reliable numerical tool for resolving transient flow structures and mixing characteristics during agitation. Recent developments in multi-relaxation-time (MRT) LBM and LBM–LES have demonstrated that mesoscopic turbulence models can accurately capture complex viscoelastic and multi-physics flow behaviors in mixer-like configurations, including double-distribution-function MRT-LBM formulations

for viscoelastic fluids and conjugate heat transfer, as well as MRT-based simulations of non-Newtonian convection and phase-change processes in complex cavities. Building on these advances, the present work targets strongly three-dimensional, twin-shaft mixing with dynamically moving boundaries and high-Reynolds-number turbulence. By simulating dynamic mixing across varying blade counts, the evolution laws of flow topology, turbulent-kinetic-energy distribution, and vorticity fields are systematically delineated with respect to time and operating conditions. On this basis, mixing dead zones and low-efficiency regions can be identified accurately, and the mechanism-level constraints on mixing efficiency can be elucidated, thereby furnishing a theoretical basis and numerical paradigm for optimizing impeller configurations and spatial layouts to jointly enhance mixing quality and reduce energy consumption.

In summary, the present work addresses the coupled dynamics of flow and mixing in enclosed domains driven by complex twin-shaft agitation, offering an in-depth exploration of the associated hydrodynamics and mixing mechanisms. The emphasis is placed on understanding and predicting the three-dimensional transient vortex systems, turbulent characteristics, and their intrinsic impacts on macroscopic mixing efficiency under diverse operating conditions. The resulting findings not only clarify the intrinsic mixing mechanisms of twin-shaft agitation but also establish a comprehensive analytical framework for performance assessment and design optimization in multi-shaft mixers, offering new perspectives and theoretical underpinnings for research and engineering practice in related fields.

2. Mathematical Model of the Mixing Process

2.1. Lattice Boltzmann Method

The lattice Boltzmann method (LBM) is a mesoscopic numerical approach derived from a discrete form of the Boltzmann equation. Its core idea is to discretize the finite-velocity space and alternate collision and streaming on lattice nodes, thereby directly evolving the particle distribution functions [21–23]. Compared with conventional computational fluid dynamics, LBM features a simple algorithmic structure and highly localized operations, and it is naturally amenable to parallel computing [24,25]. In recent years, the LBM has been widely applied to complex problems such as single- and multiphase flows, heat transfer, and porous-media transport, showing particular advantages for complex geometries, phase change, and nonequilibrium effects.

Upon discretization of the velocity space, the Boltzmann transport equation takes the form:

$$f_a(\boldsymbol{x} + \boldsymbol{e}_a\delta t, t + \delta t) - f_a(\boldsymbol{x}, t) = -\Omega_a(\boldsymbol{x}, t) + \delta t F_a(\boldsymbol{x}, t) \tag{1}$$

where f_a is the velocity distribution function, representing the probability density of a group of particles moving with a specific speed in the direction associated with index a is the position vector; x is the discrete velocity vector, and e_a is the finite set of discrete velocity modes defined in LBM, in which each e_a corresponds to a specific direction and magnitude. Fa is the discrete forcing term; Ω_a is the collision term; and Δt is the discrete time step from time t, yielding the change in the distribution function.

$$F_a = w_a\left[\frac{\boldsymbol{e}_a - \boldsymbol{u}}{c_s^2} + \frac{(\boldsymbol{e}_a \cdot \boldsymbol{u})\boldsymbol{e}_a}{c_s^4}\right] \cdot \boldsymbol{F}\left(1 - \frac{1}{2}s_\nu\right) \tag{2}$$

This formula characterizes the influence of external forces (e.g., gravity or boundary effects) on the fluid. By discretizing the forcing term, external forcing can be incorporated into the LBM framework with improved accuracy.

Specifically, w_a denotes the lattice weight, u the local fluid velocity, c_s the lattice sound speed, and F the body force (including gravity and effective forces due to moving boundaries), while s_v is the relaxation rate associated with the shear viscosity.

The present study focuses on modeling fluid convection using a multi-relaxation-time (MRT) collision operator. Within the MRT framework, the distribution function is decomposed into independent moments that correspond to distinct macroscopic quantities of the fluid, such as density, momentum, total energy, and bulk-viscosity modes. Each moment represents a specific dynamical mode of the system and is assigned an individual relaxation time according to the fluid's physical properties. By tuning these relaxation times, the evolution of the associated physical modes during collision can be effectively controlled, thereby driving the system toward equilibrium [26–29].

Compared with conventional single-relaxation-time models (e.g., the BGK scheme), the MRT model offers greater flexibility in the representation of the collision operator. It enables a finer description of the dynamics of individual macroscopic variables and, in simulations of high-Reynolds-number flows or complex fluids, delivers higher accuracy and improved numerical stability [30,31]. In the MRT collision operator, each independent moment is associated with a dedicated relaxation coefficient, which sets the rate at which the system transitions from nonequilibrium to equilibrium.

The collision operator in the MRT approach is expressed as follows:

$$\boldsymbol{m}^{\star} = \boldsymbol{m} - \boldsymbol{S}(\boldsymbol{m} - \boldsymbol{m}^{\mathrm{eq}}) + \delta t\left(\boldsymbol{I} - \frac{1}{2}\boldsymbol{S}\right)\boldsymbol{M}\boldsymbol{F}, \quad \boldsymbol{f}^{\star} = \boldsymbol{M}^{-1}\boldsymbol{m}^{\star} \tag{3}$$

where $\boldsymbol{m}$ denotes the moments (e.g., density and momentum), $\boldsymbol{m} = \boldsymbol{M}f$, $\boldsymbol{S}$ = diag (s_0, ……., s_{b-1}), $\boldsymbol{F}$ is the forcing term, $\boldsymbol{m}^{eq}$ at equilibrium represents the equilibrium moments, and the flow-field update is given by $f\ (x + e_a\delta t, t + \delta t) = f^{*}(x, t)$. **M** is the transformation matrix used in the LBM to map the velocity distribution functions into a form that is more amenable to analysis. Compared with the BGK (single-relaxation-time) scheme, the MRT method handles high-Reynolds-number flows and complex physical effects more effectively. The relaxation rate associated with the shear viscosity and the effective viscosity satisfy:

$$v = c_s^2\left(\frac{1}{s_v} - \frac{1}{2}\right)\delta t \tag{4}$$

This is the viscosity evaluation used in LBM. The relationship between the relaxation rate s_v and the effective viscosity v is corrected by the lattice sound speed c_s and the time step δt. This relation is employed to control the viscous effects of the fluid.

After computing the discrete velocity distribution functions at each spatial location, macroscopic quantities—such as pressure p, the velocity vector **u**, and the fluid density ρ—can be obtained.

$$\rho = \sum_a f_a \tag{5}$$

$$\rho\boldsymbol{u} = \sum_a \boldsymbol{e}_a f_a + \frac{1}{2}\delta t\rho\boldsymbol{F} \tag{6}$$

$$p = c_s^2\rho,\ c_s^2 = \frac{1}{3}\left(\frac{\delta x}{\delta t}\right)^2 \tag{7}$$

In the simulations, the D3Q27 lattice model is employed. In this model, each lattice node is connected to its 26 neighboring nodes, forming a complete three-dimensional cubic neighborhood. Particle populations reside only on lattice nodes; their motions are restricted to either remaining at rest or streaming along the prescribed neighboring directions to adjacent nodes. This modeling choice enables a more accurate description of particle trajectories and their interactions with the surrounding environment, thereby improving

accuracy and efficiency in multiscale and multiphysics simulations. The D3Q27 velocity set and the corresponding weights are listed below.

$$\begin{aligned} &e_0 = (0,0,0); e_{1-6} = (\pm 1,0,0),(0,\pm 1,0),(0,0,\pm 1); \\ &e_{7-18} = (\pm 1,\pm 1,0),(\pm 1,0,\pm 1),(0,\pm 1,\pm 1); e_{19-26} = (\pm 1,\pm 1,\pm 1). \end{aligned} \tag{8}$$

$$w_0 = \frac{8}{27},\ w_{1-6} = \frac{2}{27},\ w_{7-18} = \frac{1}{54},\ w_{19-26} = \frac{1}{216}. \tag{9}$$

In the discrete-velocity D3Q27 scheme, the Taylor expansion of the local fluid velocity **u** is given as follows:

$$f_{\mathrm{a}}^{eq} = \omega_{\mathrm{a}}\rho\left[1 + \frac{e_{\mathrm{a}}\cdot\mathbf{u}}{c_{\mathrm{s}}^2} + \frac{(e_{\mathrm{a}}\cdot\mathbf{u})^2}{2c_{\mathrm{s}}^4} - \frac{\mathbf{u}^2}{2c_{\mathrm{s}}^2}\right] \tag{10}$$

where $f_{\mathrm{a}}{}^{\mathrm{eq}}$ denotes the equilibrium distribution function, which describes how fluid particles are distributed over the discrete directions. It incorporates the effect of the flow velocity **u** and enables the LBE model to recover the macroscopic properties of the fluid.

2.2. LBM–LES Coupled Model

For high-Reynolds-number turbulence, standalone LBM faces notable challenges, particularly its inherent difficulty in resolving small-scale turbulent structures and strong nonequilibrium fluctuations. To improve predictive accuracy for such flows, subgrid-scale (SGS) stress modeling from large-eddy simulation (LES) has been incorporated into the LBM framework, resulting in an LBM–LES–MRT–IBM coupled model that offers several distinct advantages over conventional finite-volume CFD or LBM–RANS approaches. First, moving boundaries are handled by the immersed boundary method (IBM) without re-meshing or interpolation, eliminating numerical diffusion near rotating components. Second, the multi-relaxation-time (MRT) collision operator improves numerical stability and accuracy at high Reynolds numbers. Third, the explicit LES subgrid-scale model enables the direct resolution of transient vortical structures, including tip vortices and secondary recirculation zones, which are otherwise averaged out in RANS models. These combined features substantially enhance the framework's fidelity in capturing transient turbulent dynamics in twin-shaft mixing flows. Within this hybrid strategy, LBM resolves the macroscopic flow behavior and the evolution of large-scale vortical structures, whereas the LES-based SGS model accounts for the unresolved small-scale motions and their feedback on the resolved field [32–34]. This coupling enhances turbulence-simulation accuracy and the capture of intricate turbulent details while incurring only minimal additional computational cost. The LBM–LES method demonstrates excellent numerical stability and efficiency for complex geometries, unsteady flows, and multiscale energy-cascade phenomena. By combining the local kinetic description of LBM with the SGS modeling capability of LES, the approach mitigates mesh-dependence and dissipation-control difficulties typical of macroscopic-equation solvers, and it provides an effective meso-to-macro pathway for simulating high-Reynolds turbulence; consequently, it has emerged as a prominent direction in turbulence modeling research.

The core theoretical construct of the LBM–LES coupling is to replace the single relaxation time in conventional LBM with an effective relaxation time composed of a base (molecular-viscosity) component and an additional eddy-viscosity component that represents turbulent effects. This effective relaxation time allows the eddy-viscosity contribution to represent subgrid-scale transport, which is essential for accurately capturing small-scale fluctuations at high Reynolds numbers. Moreover, the eddy-viscosity relaxation mechanism enables the model to more faithfully reflect small-scale dissipation and backscatter effects on large-scale structures, thereby improving numerical stability and strengthening the

representation of multiscale coupled turbulence dynamics [35–39]. These features enhance the robustness and predictive accuracy of the LBM–LES model for complex turbulence, nonequilibrium flows, and strong-shear conditions, indicating broad applicability to high-speed compressible flows, near-wall turbulence, and engineering flows with pronounced separation and coherent vortices.

$$\nu_{\text{tot}} = \nu + \nu_t \tag{11}$$

$$\tau_{\text{tot}} = \frac{1}{s_\nu^{\text{tot}}} = \frac{1}{2} + \frac{\nu_{\text{tot}}}{c_s^2}\frac{1}{\delta t} \tag{12}$$

In the LBM–LES coupled model, the total relaxation time τ_{tot} represents the system's relaxation time and incorporates the effects of the molecular viscosity v and the turbulent viscosity v_t. Equation (11) specifies the evaluation of the total viscosity v_{tot}, by combining these two contributions; the model more accurately represents turbulence effects in high-Reynolds-number flows [40–42].

The total relaxation time τ_{tot} governs the rate at which the system transitions from a nonequilibrium to an equilibrium state. In the formula, the constant term adjusts the equilibrium relaxation time, whereas the second term is computed from the total viscosity v_{tot} and the time step δt.

$$\tau = \frac{1}{2} + \frac{\nu}{c_s^2}\frac{1}{\delta t} \tag{13}$$

$$\tau_t = \frac{\nu_t}{c_s^2}\frac{1}{\delta t} \tag{14}$$

where the turbulent (eddy) viscosity v_t is as follows:

$$\nu_t = (C_s\Delta)^2|\overline{S}|,\ |\overline{S}| = \sqrt{2\overline{S}_{ij}\overline{S}_{ij}} \tag{15}$$

where Cs is an empirical constant, Δ is the filter width, and $|\overline{S}|$ is the strain-rate tensor.

$$\Pi_{ij}^{\text{neq}} = \sum_a e_{a,i}e_{a,j}\left(f_a - f_a^{\text{eq}}\right) \tag{16}$$

$$\overline{S}_{ij} = -\frac{s_\nu^{\text{tot}}}{2\rho c_s^2}\Pi_{ij}^{\text{neq}} \tag{17}$$

where i and j denote two adjacent lattice nodes, $e_{a,i}$ and $e_{a,j}$ are velocity components in the discrete velocity set, f_a is the discrete distribution function, and $f_a{}^{eq}$ is the equilibrium distribution function. The non-equilibrium stress term Π_{ij}^{neq} is computed from the deviation between the distribution function and its equilibrium counterpart f_a and $f_a{}^{eq}$. Equation (16) specifies the evaluation of the non-equilibrium stress Π_{ij}^{neq}, which is based on the difference between the discrete-velocity distribution f_a and the equilibrium distribution $f_a{}^{eq}$. The quantity Π_{ij}^{neq} characterizes the stress associated with the non-equilibrium part of the flow and reflects the local shear stress under nonequilibrium conditions.

Equation (17) estimates the strain-rate tensor $\overline{S}_{ij}$ from the relationship among the non-equilibrium stress Π_{ij}^{neq}, the total relaxation time s_ν^{tot}, the density ρ, and the lattice sound speed c_s, thereby characterizing the shear effects during fluid flow [43–46].

Where the SGS (subgrid-scale) relaxation rate s_ν^{SGS} and the total relaxation rate s_ν^{tot} are updated as:

$$s_\nu^{\text{SGS}} = \frac{1}{\tau_t} = \frac{c_s^2}{\nu_t}\delta t \tag{18}$$

$$s_\nu^{\text{tot}} = \frac{1}{\tau_{\text{tot}}} \tag{19}$$

Equation (18) couples the SGS relaxation rate with the turbulent viscosity v_t and the lattice sound speed c_s, thereby describing how the time step δt, influences the relaxation

rate within the turbulence model. Equation (19) provides the update for the total relaxation rate s_ν^{tot}, which is linearly related to the total relaxation time τ_{tot}.

Smagorinsky proposed one of the earliest subgrid-scale models, the Smagorinsky model, in 1963 [47]:

$$\tau_{ij}^{\mathrm{SGS}} - \frac{1}{3}\tau_{kk}^{\mathrm{SGS}}\delta_{ij} = -2\nu_t \overline{S}_{ij} \tag{20}$$

where τ_{ij}^{SGS} denotes the subgrid-scale (SGS) stress, τ_{kk}^{SGS} represents the shear stress in turbulent flow, δ_{ij} is the trace of the SGS stress tensor—which quantifies the volumetric (isotropic) stress—and δ_{ij} is the identity tensor used to ensure that the isotropic correction remains consistent in all directions.

Smagorinsky refined the subgrid eddy-viscosity coefficient, expressing it in the following form:

$$\nu_t = (C_s\Delta)^2\sqrt{2\overline{S}_{ij}\overline{S}_{ij}} \tag{21}$$

where *Cs* denotes the Smagorinsky constant, typically taking values in the range 0.1–0.2, as shown below.

$$C_s(y^+) = C_{s0}\left[1 - \exp\left(-\frac{y^+}{A^+}\right)\right]^2 \tag{22}$$

Equation (22) describes a near-wall correction to the Smagorinsky eddy viscosity, ensuring a more accurate representation of the flow behavior near walls in high-fidelity simulations.

Where *y+* is the wall-normal distance in wall units, C_{s0} is a constant typically taken as the Smagorinsky constant, and *A+* is an empirical constant. The turbulent viscosity v_t in the Wall-Adapting Local Eddy-viscosity (WALE) model is given by:

$$\nu_t = (C_w\Delta)^2\frac{\left(S_{ij}^d S_{ij}^d\right)^{3/2}}{\left(\overline{S}_{ij}\overline{S}_{ij}\right)^{5/2} + \left(S_{ij}^d S_{ij}^d\right)^{5/4}}\begin{pmatrix}1 & 0\\ 0 & 1\end{pmatrix} \tag{23}$$

where C_w is the constant in the WALE model, Δ and is the filter width. S_{ij}^d denotes the strain-rate tensor as defined in WALE, which evaluates the local shear strain of the fluid; $\overline{S}_{ij}$ denotes the conventional strain-rate tensor that characterizes the fluid's shear strain.

$$\overline{S}_{ij} = \frac{1}{2}\left(\partial_i u_j + \partial_j u_i\right),\ g_{ij} = \partial_j u_i \tag{24}$$

$$S_{ij}^d = \frac{1}{2}\left(g_{ik}g_{kj} + g_{jk}g_{ki}\right) - \frac{1}{3}\delta_{ij}g_{kl}g_{lk} \tag{25}$$

where u_i and u_j are the velocity components, $б_i u_i$ and $б_j u_j$ denote the spatial derivatives of the velocity components, $g_{ij} = б_j u_{ji}$ is the velocity-gradient tensor, and δ_{ij} is the Kronecker delta, used to extract the diagonal components of the strain-rate tensor.

The overall coupled formulation under the MRT collision operator in the LBM–LES model is as follows:

$$\boldsymbol{m}^\star = \boldsymbol{m} - S(s_\nu^{\mathrm{tot}})(\boldsymbol{m} - \boldsymbol{m}^{\mathrm{eq}}) + \delta t\left(\boldsymbol{I} - \frac{1}{2}S\right)\boldsymbol{MF} \tag{26}$$

where $S(s_\nu^{\mathrm{tot}})$ is the relaxation operator constructed from the total relaxation rates s_ν^{tot}, it governs the relaxation of the macroscopic moments toward their equilibrium values.

Building on the foregoing formulations, turbulence can be characterized more accurately within the LES framework, particularly in near-wall regions and high-gradient flows. Compared with the Smagorinsky model, the WALE formulation explicitly incorporates a more refined representation of the velocity-gradient tensor and local strain features. Consequently, it exhibits superior applicability both in the low-speed viscous sublayer

near the wall and in strongly turbulent regions. With these enhancements, the WALE model enables more robust capture of the dominant scales and local shear structures in complex flows within LES. It reduces the systematic biases of traditional models in high-gradient zones, thereby improving the fidelity of near-wall representation and the overall predictive consistency.

In comparison with conventional finite-volume CFD using sliding or overset meshes and RANS closures, the present LBM–LES–MRT–IBM framework offers distinct computational and physical advantages. (i) Moving boundaries are treated directly within a fixed Cartesian lattice without re-meshing or interpolation, ensuring continuous force exchange across the fluid–solid interface; (ii) the MRT collision operator enhances numerical stability at high Reynolds numbers and mitigates spurious oscillations; (iii) explicit LES subgrid modeling enables the capture of transient vortical structures, such as tip vortices and secondary recirculation loops, which are typically averaged out by RANS models. These improvements collectively yield higher fidelity in transient turbulence resolution and superior robustness for strongly unsteady flows.

3. Numerical Simulation of the Mixer Device

3.1. Geometric Model

The geometric model of the mixer is established in a three-dimensional Cartesian coordinate system to accurately simulate the internal flow field and mixing characteristics. A reference point on the vessel's central axis is set as the origin; the z axis extends vertically upward along the main shaft, and the x and y axes are orthogonal and lie in the mid-plane of the vessel. The vessel is a right circular cylinder with an inner diameter of 200 mm and a height of 280 mm. The complete geometry and arrangement are shown in Figure 1. For boundary conditions, the inner wall is treated as a no-slip solid wall to reflect the near-wall velocity distribution. To accommodate different stages of the study, the thermal boundary can be switched between isothermal and adiabatic to examine heat transfer under a fixed wall temperature and, respectively, temperature evolution and energy distribution under adiabatic conditions. The drive and blade configuration is as follows: a central main shaft of 20 mm diameter runs from the bottom and connects to an auxiliary shaft of 50 mm diameter; two side shafts of 10 mm diameter extend symmetrically from the auxiliary shaft, each carrying two blades to intensify local shear and recirculation. A horizontal impeller of 120 mm diameter is mounted on the main shaft, consisting of four blades with rectangular cross-sections. All blades are installed at a 60° inclination relative to the horizontal plane, and adjacent blade sets are separated by a vertical spacing of 70 mm. This combined design of inclination and spacing effectively disrupts symmetric flow patterns and strengthens axial and radial mixing, thereby improving overall mixing efficiency. The model provides a reliable geometric basis for subsequent studies of multiphase flow, energy transfer, and mixing mechanisms.

3.2. Initial and Boundary Conditions

In simulations of mixer flow fields, the appropriate specification of initial and boundary conditions is decisive for ensuring accuracy and physical fidelity. Unlike classical finite-volume or finite-element schemes governed by the continuum hypothesis and the Navier–Stokes equations, the LBM employed herein describes fluid behavior at the mesoscopic scale. It reconstructs macroscopic flow features through the evolution and collision of particle distribution functions, combining clear physical underpinnings with high algorithmic parallelism [48–51]. The D3Q27 discrete-velocity model is adopted, which prescribes 27 discrete velocity directions in three dimensions. Compared with the commonly used D3Q15 and D3Q19 models, it offers a higher degree of velocity discretization, markedly im-

proving isotropy accuracy and enhancing the resolution of complex turbulent features such as vortex evolution and energy cascades. This model is particularly suitable for flows with strong shear, rotational symmetries, and pronounced unsteadiness—for example, the multi-shaft mixing flow considered here—where unsteady disturbances and complex vortex systems induced by multiple rotating components impose stringent accuracy requirements.

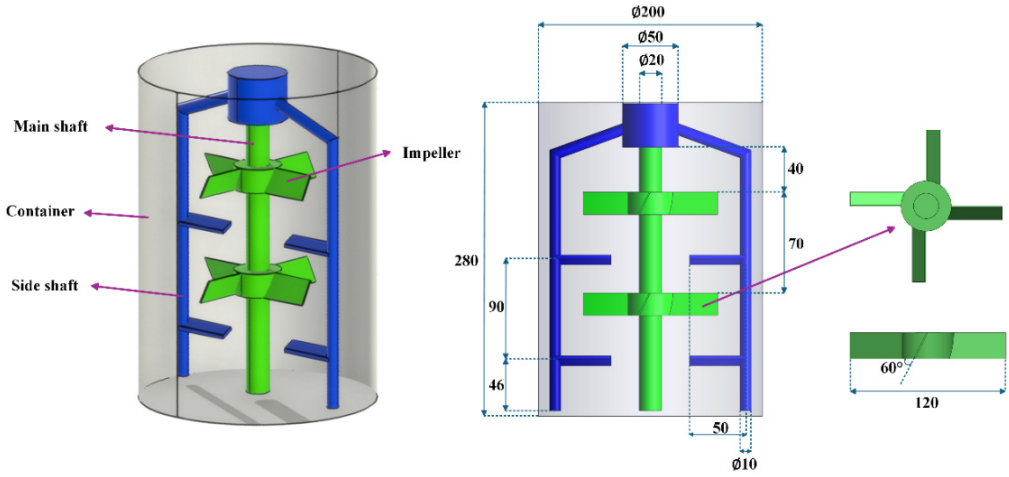


Figure 1. Geometric model of the mixer and detailed dimensions.

For spatial discretization, a particle–volume grid system within a Lagrangian framework is employed, which effectively circumvents meshing difficulties posed by complex geometries and improves adaptability to moving boundaries and geometric deformation [52–54]. The mesh model of the mixer is showed in Figure 2. In the mixer considered—which comprises a main shaft and multiple side shafts rotating concurrently—all rotating components spin about their respective axes at prescribed constant speeds. The interaction between the rotating parts and the surrounding fluid is handled using the immersed boundary method (IBM). IBM embeds moving boundaries into a fixed background grid and accurately represents momentum exchange between the rotating components and the fluid, thereby enabling effective capture of local turbulence evolution, instantaneous shear-layer distribution, and energy-dissipation characteristics arising from solid–fluid coupling, and providing a reliable numerical tool and theoretical basis for in-depth understanding of complex flow mechanisms in multi-shaft mixers.

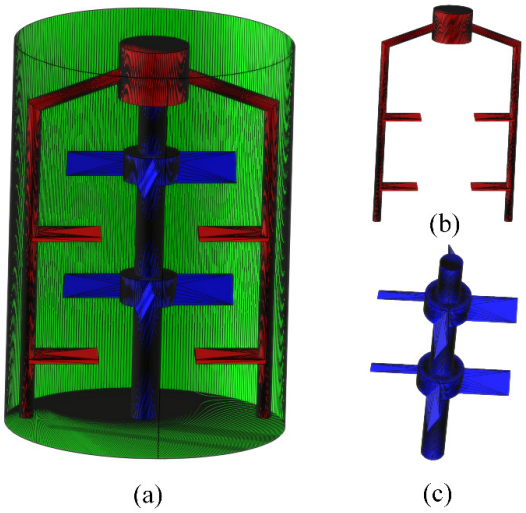


Figure 2. Mesh model of the mixer. (**a**) Overall mesh. (**b**) Impeller 1. (**c**) Impeller 2.

Across the entire computational domain, the external body force is prescribed to conform strictly to the physical scenario. The gravitational field is defined as a vertical gravitational acceleration, specified as $-9.81\ \mathrm{m{\cdot}s^{-2}}$ in the z axis direction. This specification faithfully represents the persistent influence of gravity on the fluid system and provides a realistic mechanical environment for subsequent studies of buoyancy-driven flows, density stratification, and particle settling. The fluid initially remains at rest, with all macroscopic velocity components set to zero throughout the domain. The earlier placeholder value of "$-10\ \mathrm{m{\cdot}s^{-1}}$" referred only to an internal normalization in the LBM code and did not represent a physical inflow. In the present implementation, the flow evolves naturally from rest under the action of impeller rotation and gravity, consistent with typical startup conditions in industrial mixers. This clarification ensures that the initialization is physically meaningful and avoids potential misinterpretation. This configuration reproduces the physical process in which the fluid evolves from complete rest in practical mixing operations, avoids introducing nonphysical perturbations or preimposed flow patterns, and furnishes a clear baseline for examining transient evolution during flow startup. The initial distribution of the liquid region is defined via a coordinate-based mathematical expression, ensuring that at the simulation onset the liquid occupies only the prescribed geometric region, as given by the following function:

$$((x^2 + y^2) < 0.1^2) * (z < 0.22) * (z > 0.005) \tag{27}$$

The geometric model comprises three solid components of distinct shapes, whose position is constrained to be fixed in the x, y, and z directions, thereby ensuring that the objects are located at the origin at the initial time.

$$if((t < 0.001) * (t > 0) + (t = 0), 100000 * t * t, 200 * t - 0.1) \tag{28}$$

$$if((t < 0.001) * (t > 0) + (t = 0), 105000 * t * t, 210 * t - 0.105) \tag{29}$$

In simulation studies, the accurate specification of boundary conditions is critical to ensuring the physical fidelity of the computed flow field. For the vessel walls, a fixed wall boundary condition is imposed, under which the walls remain stationary throughout the computation. An adaptive wall model—automatically recommended according to the flow characteristics—is employed to preserve accuracy while improving computational efficiency. Specifically, the wall roughness is set to 0 m, implying ideally smooth surfaces for all walls. This setting accords with the typical manufacturing tolerance of laboratory stainless-steel vessels and avoids roughness-induced local turbulence that could distort the main flow structure, thereby keeping the results focused on the mixer-driven flow features. Water is used as the liquid working fluid and air as the gaseous medium. The key thermophysical parameters of each phase, evaluated at a standard temperature of 288.15 K and atmospheric pressure, are listed in Table 1.

Table 1. Material parameters.

	Density $\mathbf{kg{\cdot}m^{-3}}$	**Dynamic Viscosity** $\mathbf{Pa{\cdot}s}$	**Coefficient of Heat Conductivity** $\mathbf{W{\cdot}(m{\cdot}K)^{-1}}$	**Specific Heat** $\mathbf{J{\cdot}(kg{\cdot}K)^{-1}}$
Air	1.225	1.7894×10^{-5}	0.0243	1006.43
Water	998.3	0.001	0.58	4182

The initial temperature field of all fluids in the computational domain is uniformly set to 288.15 K, corresponding to the standard temperature used in Table 1, and the initial static pressure field over the entire domain is initialized to 0 Pa relative to atmospheric pressure. This configuration mimics an open-to-atmosphere pressure boundary for an

open vessel and ensures both numerical stability and physical plausibility in the pressure solution. All solid-wall boundaries are prescribed as ideally smooth surfaces with the roughness parameter set explicitly to zero, thereby avoiding the complex influence of wall microstructures on near-wall flow. The total simulation time is 2 s, which preliminary tests confirm is sufficient to capture the full flow-field evolution from the startup transient to quasi-steady operation. The total simulation time is 2 s, which preliminary tests confirm is sufficient to capture the full flow-field evolution from the startup transient to quasi-steady operation [55–57]. Regarding output, the data-saving frequency is synchronized with the solver time step, yielding an effective sampling rate of 50 Hz. This ensures complete and continuous recording of transient flow details, meeting the data requirements for subsequent vortex-structure identification and spectral analysis. For spatial discretization, a uniform mesh is employed to balance computational cost against resolution requirements. Mesh seeding and domain-wide discretization are performed automatically by the solver, ensuring consistent mesh quality and reliable numerical solutions, thereby providing a robust numerical basis for the accuracy and efficiency of the overall flow simulation.

3.3. Grid-Independence Verification

To ensure the accuracy and reliability of the numerical results, grid-independence verification is required for the computational model. The grid density critically affects both solution accuracy and computational efficiency: an excessively fine grid improves resolution but markedly increases resource usage and wall time, whereas an overly coarse grid fails to capture complex flow physics and thus distorts the results [58–60]. Although a meshless Lagrangian particle method is employed here—eschewing conventional structured or unstructured meshing—its accuracy is still constrained by the particle resolution, i.e., the equivalent mesh size. Accordingly, the sensitivity of the results to the discretization scale is assessed by systematically varying the particle resolution and conducting comparative analyses, thereby verifying whether the solution is mesh independent. The stability coefficient is adopted as the evaluation metric for grid-independence verification. By comparing its temporal trends under different particle resolutions, convergence of the numerical solution can be ascertained and an appropriate simulation resolution identified to ensure reliability, as shown in Figure 3.

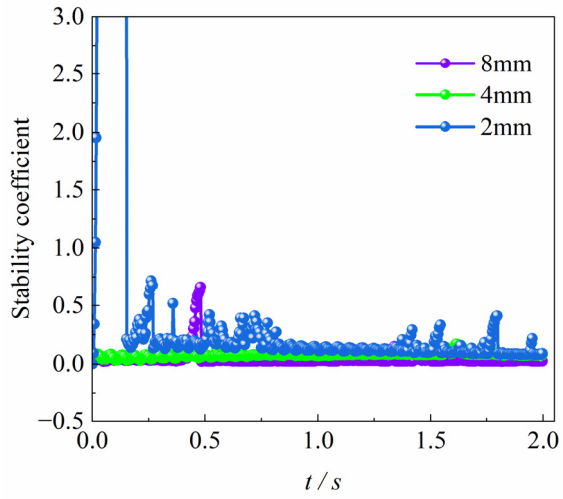


Figure 3. Grid-independence verification.

A comprehensive analysis of the time histories of the stability coefficient for various grid sizes reveals a pronounced impact of discretization scale on numerical stability and computational efficiency. Specifically, the 8 mm grid incurs the lowest computational cost

but exhibits small oscillations over 0.4–0.5 s, with a peak value of 0.65, indicating clear deficiencies in capturing flow details and maintaining numerical stability. By contrast, the 2 mm grid shows extremely strong unsteady fluctuations during the initial stage (0–0.2 s), with the instantaneous stability coefficient exceeding 3.0. Although the amplitude diminishes in later intervals (0.2–0.6 s and 1.4–1.8 s), persistent high-frequency oscillations remain, further evidencing limited robustness in practical simulations. In contrast, the 4 mm grid exhibits the smoothest, convergent evolution throughout the entire period, while requiring only 60% of the wall-clock runtime (the actual elapsed real time measured on the workstation, as opposed to CPU time per core) of the 2 mm grid. This demonstrates an optimal compromise between numerical stability and computational economy. Based on quantitative comparisons, a 4 mm grid is ultimately selected for subsequent hydrodynamic simulations to obtain stable and reliable solutions with a reasonable computational budget.

To validate the accuracy of the transient solution model based on the LBM–LES method adopted in this study for characterizing unsteady vortex structures and energy evolution, both quantitative and qualitative comparisons were performed. The total kinetic energy and total enstrophy (vorticity pseudo energy) shown in Figure 4 serve as two global indicators that reflect the time-accumulated intensity of the velocity field and the overall vortical behavior. Since experimental data for the specific twin-shaft configuration are unavailable, a benchmark comparison is made against the well-established CFD study of Wang [13]. on a dual-shaft eccentric mixer. The growth, peak, and saturation trends of both quantities agree closely between the present LBM–LES and the reference CFD, confirming the fidelity of the proposed model. Additionally, representative cross-sections of velocity magnitude and turbulence intensity were compared with the MRF-based solution, showing that the main recirculation loops and high-shear zones coincide within expected numerical tolerance. We acknowledge that full pointwise experimental validation is beyond the scope of this study and explicitly state this as a limitation in the discussion.

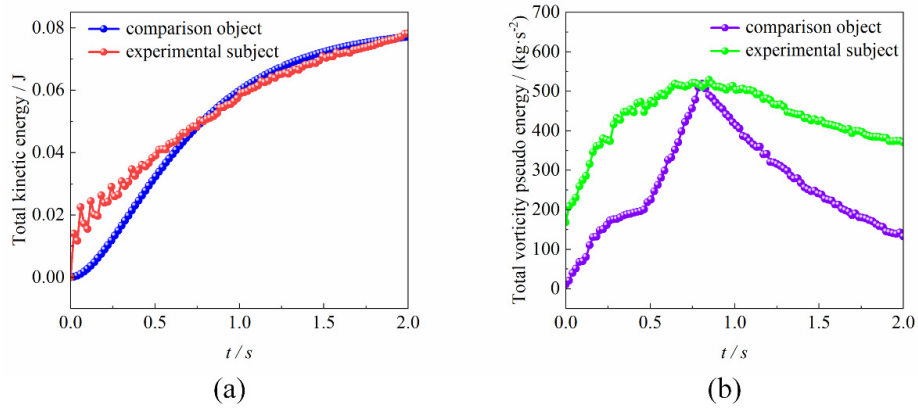


Figure 4. Comparative verification. (**a**) Comparison of total kinetic energy. (**b**) Comparison of total vorticity energy.

Total kinetic energy serves as a cumulative representation of macroscopic flow intensity and is particularly sensitive during the start-up and acceleration phases; total enstrophy, as an integral measure of vortical strength, intuitively reveals the generation, maintenance, and dissipation of vortex structures. As shown in Figure 4a, both total kinetic energy curves exhibit an overall monotonic increase from the initial moment and tend to converge after approximately 2.0 s, indicating gradual saturation of the macroscopic kinetic energy with agitation. The present model shows minor oscillations in the initial stage, followed by a rapid climb, whereas the comparative model displays a smoother curve. This difference can be attributed to the high-resolution capture of tip vortex generation, shedding, and circumferential unsteady shear effects by the LBM-LES method, which makes it more

sensitive to transient flow during the start-up phase; in contrast, the MRF method, based on the "frozen rotor" quasi-steady assumption, results in a milder response in the same stage. Figure 4b indicates that both models reach the peak total enstrophy at around 0.9 s, reflecting a generally consistent timescale for vortex establishment. However, after the peak, the present model decays slowly and maintains a higher level between 1.0 and 2.0 s, whereas the comparative model decays almost linearly and rapidly. The higher and more sustained enstrophy indicates that the present solution preserves stronger shear effects and vortex structures throughout the domain, a conclusion well supported by the turbulent kinetic energy and vorticity evolution contours provided in the paper.

Both schemes eventually reach similar levels in terms of macroscopic kinetic energy, but exhibit significant differences in their response to unsteady flow during the start-up to transition phase: the present model displays early minor oscillations and a faster rise rate, reflecting higher sensitivity to transient flow structures. In terms of vortex strength and persistence, the present simulation demonstrates higher and more sustained global enstrophy, while the comparative model shows a rapid decay trend after reaching the peak. These differences align with the approach emphasized in the comparative literature that "characterizes mixing efficiency through shear and energy input," further underscoring the importance of accurately resolving transient vortex structures in dual-shaft agitation systems for elucidating the intrinsic relationship between energy transfer and mixing efficiency.

4. Results and Discussion

4.1. Mixing-Flow Mechanisms Based on LBM–LES

4.1.1. Pressure Characteristics of the Mixing Flow Field

As shown in Figure 5, a contour map of static pressure on a vertical cross-section is presented for the four-blade mixer under representative operating conditions. The distribution clearly reveals the nonuniform nature of the pressure field during mixing; its magnitude gradients and spatial patterns directly reflect the hydrodynamic effects induced by blade rotation and the associated energy-input characteristics. To faithfully represent variable-speed operation encountered in practice, a piecewise speed-control function is introduced to adjust the impeller rotational speed in stages according to time intervals of the variable t. This setup effectively reproduces start–stop and speed-ramp transients typical of industrial scenarios, thereby enabling more realistic capture of evolving flow structures and their impact on mixing performance.

$$\text{speed}(t) = \begin{cases} 105000\ t^2, & 0 \le t < 0.001 \\ 210\ t - 0.105, & \text{otherwise} \end{cases} \tag{30}$$

In the startup control strategy of the main shaft, the time variation in the speed is precisely regulated by a piecewise function. For $0 \le t < 0.001$ s, the shaft speed follows a quadratic law, v = 105,000·t^2. This design, via the square-law increase in speed in the initial stage, ensures a continuous and smooth transition of acceleration, thereby markedly reducing the risk of mechanical impact and system instability caused by abrupt speed changes. When $t > 0.001$ s, the speed regulation switches to a linear ramp, $v = 210t - 0.105$. The linear segment helps maintain predictable speed variation and control stability once the shaft enters normal operation, thereby supplying a reliable rotational-speed boundary condition for the subsequent flow simulation. Overall, the piecewise strategy balances smoothness during startup with controllability during operation, reflecting an orderly guidance of the system dynamics. The piecewise rotational-speed function in Equation (30) corresponds to a characteristic angular velocity of approximately 210 rad·s^{-1} at the end of

the ramp, which—given the impeller diameter of 0.12 m and water properties—yields an impeller Reynolds number of $Re = \frac{\rho \omega D^2}{\mu} \approx 3.0 \times 10^5$. This value lies well within the fully turbulent regime typical of industrial liquid mixing operations, validating the use of the LES framework and ensuring that the simulated conditions are representative of realistic high-Reynolds-number mixing processes.

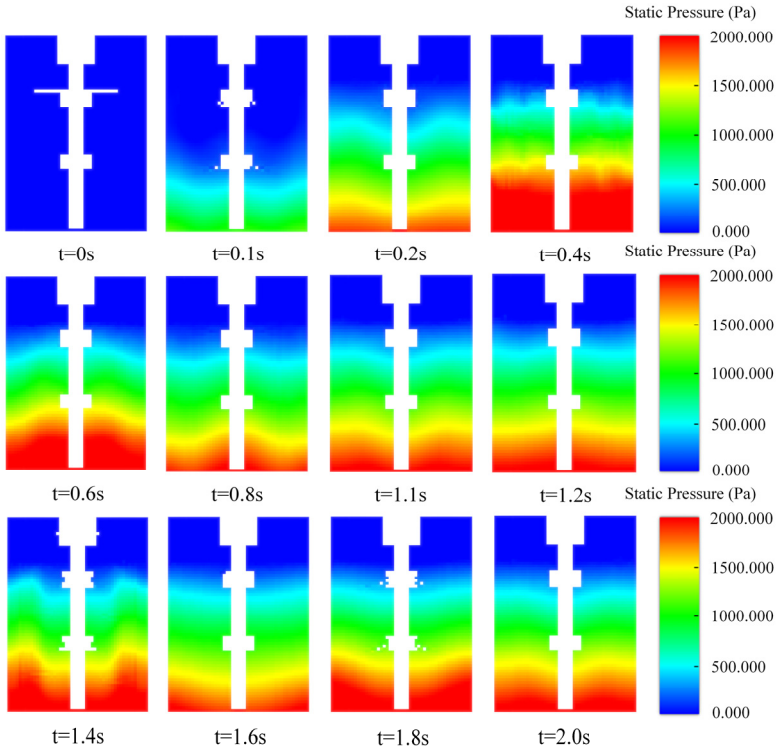


Figure 5. Vertical-section static-pressure contours.

According to the static-pressure contours in Figure 5, the internal pressure field of the mixer exhibits an overall spatially uniform character. Analyzing the static-pressure field at successive instants from t = 0 to t = 2.0 s clearly reveals the dynamic evolution of the flow during mixing. All snapshots use a unified color scale, with blue denoting 0 Pa (low pressure) and red 2000 Pa (high pressure); the continuous gradient reflects spatial variations in pressure magnitude. As mixing proceeds, persistent interactions between the fluid and internal structures lead to pronounced spatiotemporal evolution of the pressure field. At key instants such as t = 1.1 s and t = 1.8 s, hydrodynamic effects become especially prominent, with localized regions of markedly elevated pressure—visible as concentrated red zones—indicating the specific influence of transient structures, including blade-induced flow and vortex shedding, on the pressure field. These dynamic visualizations provide essential evidence for further understanding the unsteady flow characteristics within the mixer.

4.1.2. Planar Velocity-Distribution Patterns of the Mixing Flow

Figure 6 presents a sequence of planar velocity contours for the four-blade mixer over the entire startup and operating period. The analysis indicates that the flow field exhibits a high degree of symmetry, and its temporal evolution agrees well with theoretical expectations. In the initial stage, the fluid is at rest; the field appears uniformly blue, indicating velocities close to zero. As mixing proceeds, blade rotation accelerates the fluid and produces pronounced spatial differentiation in the velocity field: near the main shaft, speed variations remain modest and the flow is relatively uniform. Near the side shafts,

however, velocity gradients are large; at t = 0.6 s, 1.4 s, and 1.6 s, local velocities increase markedly, reflecting strong shear and acceleration effects. During the development stage, a blade-driven recirculating structure gradually emerges, which is the key mechanism enabling material mixing. By the stabilization stage, the velocity field approaches dynamic equilibrium: high-speed regions remain localized near the blade tips, whereas low-speed regions occupy the mixer center and near-wall zones, yielding a clear and stable global flow pattern.

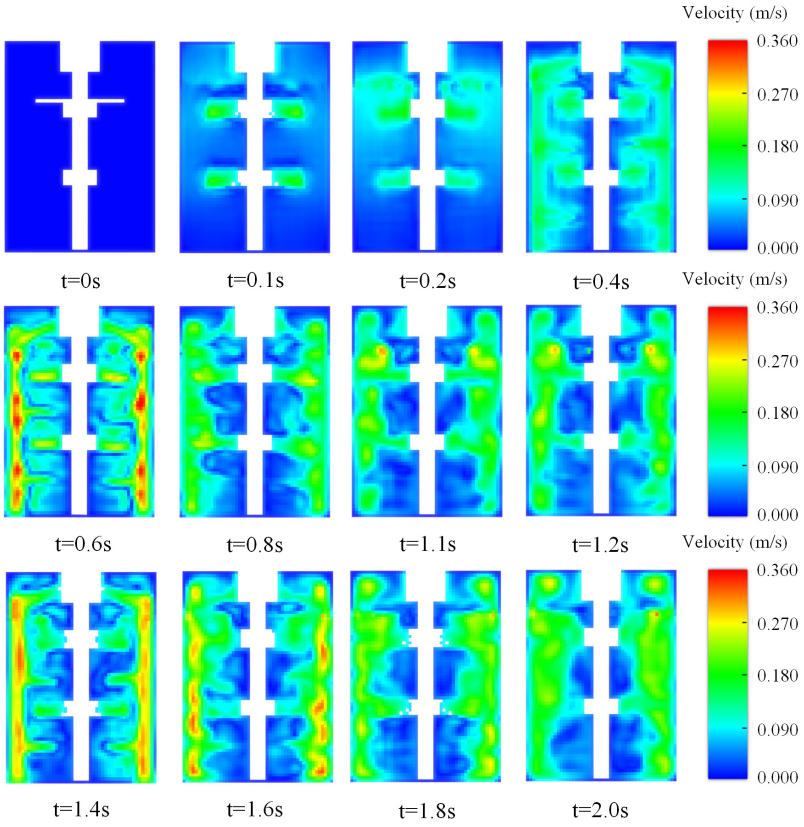


Figure 6. Vertical-section velocity contours.

4.1.3. Analysis of Turbulent Kinetic Energy Characteristics in the Mixing Flow

Figure 7 presents a sequence of turbulent kinetic energy (TKE) contours on a vertical section and on the horizontal plane at z = 0.1 m, systematically documenting the temporal evolution of turbulence intensity from the initial instant to the stabilized mixing stage. The color gradient visualizes the spatial distribution of TKE, with blue indicating low values and red denoting high values, thereby depicting the complete process of turbulence generation, development, and dissipation during mixing. At the initial stage, the TKE field is relatively uniform and predominantly blue, indicating that the fluid has not yet experienced strong perturbations. As mixing proceeds, a pronounced spatial differentiation of turbulent structures emerges: near the impeller blades—especially in the blade–fluid contact zones at the tips. These high-TKE regions reflect intense shear and velocity gradients, marking the primary sites where mechanical energy is converted into turbulence. Further analysis indicates that the formation of high-TKE zones is closely tied to vortical structures induced by blade rotation; as these vortices shed and evolve, they continuously dissipate energy and substantially enhance lateral entrainment and momentum exchange.

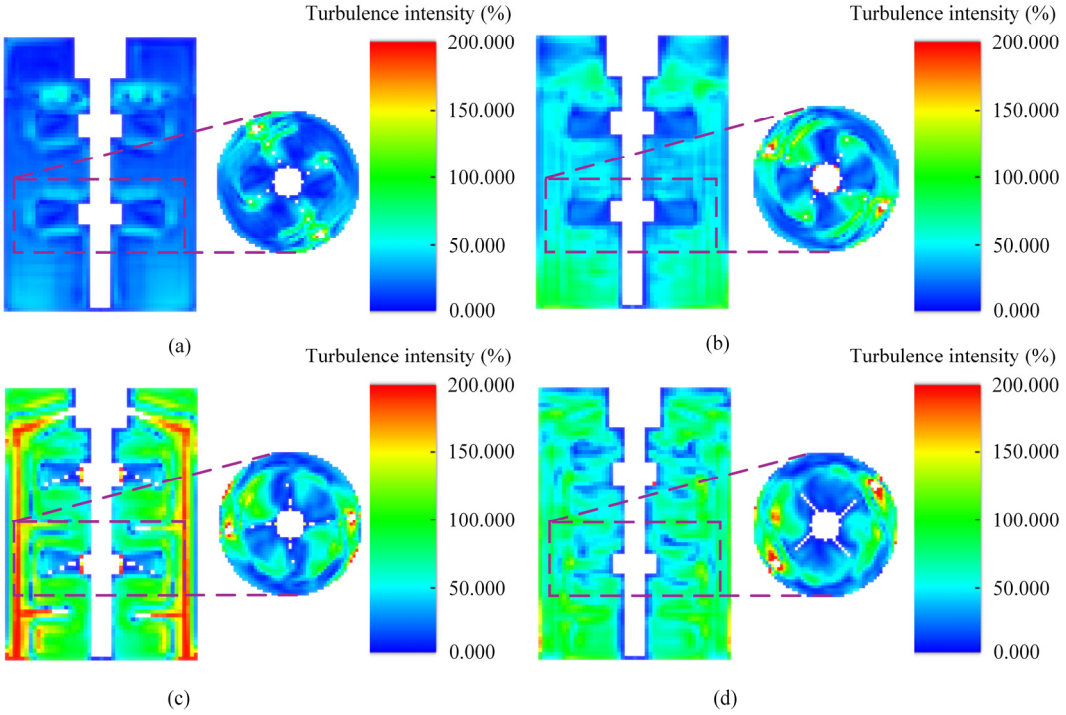


Figure 7. Evolution of TKE in the mixer flow field. (**a**) 0.16 s, (**b**) 0.32 s, (**c**) 0.48 s, (**d**) 0.64 s.

As time advances, the TKE distribution follows a clear evolution path: it originates in the upper-left region, progressively extends rightward, subsequently forms a stable high-turbulence band in the lower-left region, and ultimately completes the construction of the turbulent structure in the lower-right region. This dynamic process reveals the complexity of the unsteady flow inside the mixer and corroborates the close linkage between turbulence production and the blade motion trajectory. Notably, on the horizontal section at z = 0.1 m, the TKE distribution exhibits finer spatial structures, providing an important complement to the understanding of the three-dimensional turbulent field. From an engineering perspective, these high-TKE regions are critical to mixing efficiency and mass-transfer rate during agitation. Their magnitude and spatial coverage closely correlate with the local power input and thus with the impeller Reynolds number. Regions of elevated TKE—particularly near blade tips and side-shaft impellers—correspond to zones of intense mechanical energy dissipation. In stirred vessels of fixed geometry, the characteristic turbulent velocity scale is of order $u' \sim ND$, such that the turbulent kinetic energy satisfies $k \sim (ND)^2$ and the mean dissipation rate scales as $\varepsilon \sim N^3D^2$, while the shaft power input follows the classical relation $P \sim \rho N^3 D^5$ for a given fluid. Consequently, the contour levels observed in Figure 7 increase monotonically with the impeller Reynolds number $\mathrm{Re} = \rho ND^2/\mu$ and with the normalized power input, up to the point where inter-blade interference limits the effective transfer of kinetic energy. In this regime, increasing blade number or speed strengthens the high-TKE zones near blade tips and side-shaft impellers but also promotes overlap of adjacent shear layers, which explains the saturation and partial redistribution of TKE at the highest blade counts. These quantitative relationships strengthen the physical interpretation of the TKE fields and confirm that the present LBM–LES framework captures the coupling between power input, Reynolds number, and turbulence intensity with high fidelity.

4.1.4. Analysis of Vorticity Evolution in the Mixing Flow

Figure 8 systematically presents vorticity-field contours on a vertical section and on the z = 0.1 m horizontal section at four representative instants (0.16 s, 0.32 s, 0.48 s, and 0.64 s).

This sequence documents the spatiotemporal evolution of vortical structures throughout the mixing process and provides essential evidence for understanding the rotational characteristics and energy-transport mechanisms of the internal flow. A comparative analysis of the vorticity distributions at different times clearly reveals the dynamic evolution of the vorticity field within the mixer. At the initial stage, the vorticity distribution is relatively uniform, indicating that the fluid has only begun to respond to blade rotation. As the process advances, pronounced high-vorticity regions develop around the blades, corresponding to strong velocity gradients and shear. In particular, near the blade tips and edges, intensified relative motion between the fluid and solid surfaces markedly elevates local vorticity, exhibiting typical boundary-layer separation features. The emergence of these high-vorticity zones furnishes the necessary conditions for the generation and development of vortical structures.

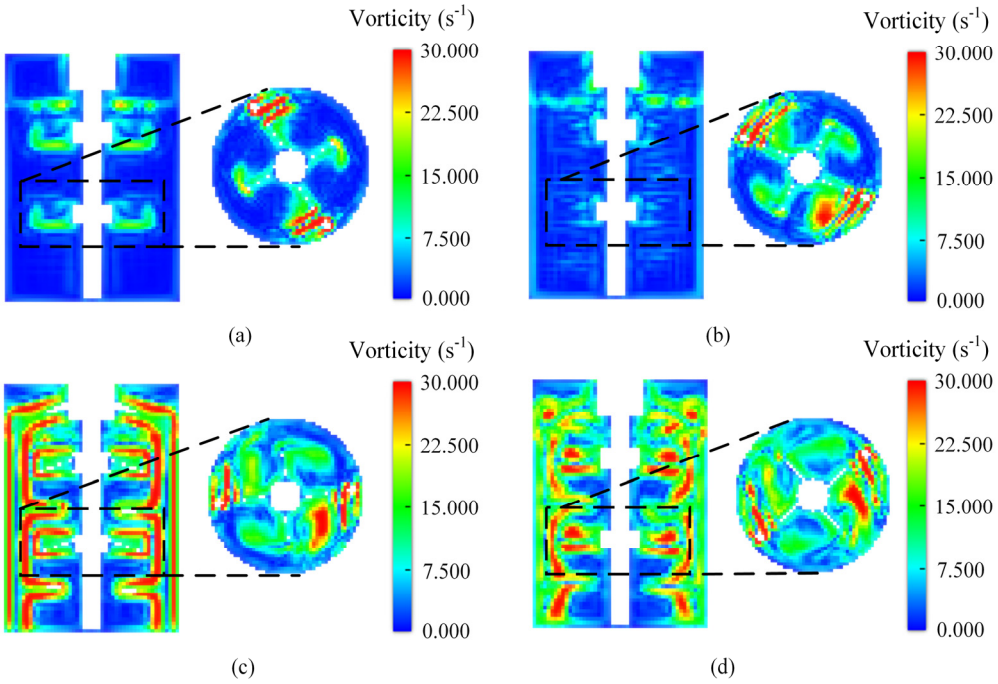


Figure 8. Evolution of the vorticity field in the mixer flow. (**a**) 0.16 s. (**b**) 0.32 s. (**c**) 0.48 s. (**d**) 0.64 s.

On the horizontal section at z = 0.1 m, the spatial distribution of vorticity clearly reveals the internal recirculating flow patterns. High-vorticity regions align predominantly with the fluid's dominant flow paths, especially within the blade-swept zones and the boundary-layer regions near the vessel wall. These high-vorticity bands correspond to vigorous vortex-production zones in which fluid microelements undergo complex rotation and deformation. From 0.16 s to 0.64 s, the vorticity field evolves from localized concentrations toward a more global distribution, reflecting the diffusion and transport of vortical structures within the flow. Further analysis shows that the evolution of the vorticity field is closely linked to energy transfer during mixing. The high-vorticity zones not only mark regions where mechanical energy is converted into turbulent kinetic energy but also indicate the intensity distribution of vortical motion. On vertical sections, the blade-induced primary vortices and their accompanying secondary vortex systems are clearly identifiable, with their interaction zones often corresponding to peak vorticity. At t = 0.48 s and 0.64 s, in particular, the vorticity field exhibits complex spatial organization, indicating that the flow has developed into a fully three-dimensional turbulent state.

The spatiotemporal characteristics of the vorticity distribution are of fundamental importance for elucidating the mixing mechanisms of the mixer. Quantitative analysis

of the vorticity field enables optimization of mixer geometry and operating parameters, minimizing energy consumption while maintaining mixing performance. By systematically revealing the evolution of the vorticity field, this study provides essential theoretical guidance and data support for the optimal design of mixing equipment.

4.2. Evolution Characteristics of the Mixing Flow with Different Numbers of Blades

In this study, to systematically investigate how blade number governs the internal flow features of the mixer, a series of numerical simulations is conducted under a controlled-variable framework, wherein all other geometric parameters are held constant and the impeller is configured with 2, 4, 6, and 8 blades, respectively. By systematically comparing the spatiotemporal distributions of these two flow-field metrics across blade-number configurations, we elucidate the mechanisms by which blade count affects the flow-field structure, energy-transport efficiency, and overall mixing performance, thereby providing theoretical guidance and data support for mixer optimization.

4.2.1. Turbulence-Intensity Analysis for Different Blade Numbers

Turbulence intensity is a key dimensionless parameter that characterizes turbulent fluctuations. In physical terms, it reflects the severity of vortex-structure evolution and the energy cascade in the flow field, serving as an important indicator of flow regime and turbulence development. However, turbulence intensity does not exhibit a simple monotonic correspondence with impeller efficiency. Nevertheless, it effectively captures the amplitude of pressure fluctuations induced by unsteady phenomena such as vortex shedding and flow separation. Accordingly, turbulence intensity serves as an important reference for assessing flow stability, predicting pressure-fluctuation characteristics, and diagnosing energy-loss mechanisms in mixer performance analysis and design optimization.

A systematic comparison of the turbulence-intensity contours for different blade counts reveals a pronounced influence of blade number on the internal turbulent structures and their spatial distribution, as shown in Figure 9. As the blade count increases from 2 to 8, the spatial distribution of turbulence intensity becomes conspicuously more complex and nonuniform. Specifically, with two blades, the distribution is relatively simple, with high-intensity regions confined mainly to the near field of the blades, indicating a limited disturbance extent and a comparatively singular turbulence-production mechanism. In contrast, the eight-blade configuration displays a broader distribution with overall higher intensities; multiple high-turbulence regions emerge simultaneously and interact, demonstrating that increasing blade number indeed enhances turbulence production and, in principle, mixing efficiency. However, this enhancement is accompanied by substantially higher energy consumption; the increased flow resistance associated with a dense blade arrangement can intensify viscous dissipation and, in turn, pose a risk of localized overheating. For intermediate configurations, the four- and six-blade designs exhibit turbulence-intensity distributions that lie between these two extremes. Notably, the four-blade configuration achieves a particularly favorable balance: it maintains sufficient spatial coverage and intensity to ensure effective entrainment and mass transfer while avoiding the excessive energy expenditure associated with larger blade counts. As evident in Figure 9, its turbulence field is comparatively uniform, promoting coherent circulation throughout the mixing domain and thereby enabling an efficient and stable mixing process. Moreover, a moderate blade count mitigates local energy accumulation and effectively limits temperature rise due to viscous dissipation, which is of practical importance for maintaining material chemical stability and ensuring operational safety. Considering turbulence-intensity patterns alongside energy efficiency and thermal manage-

ment, the four-blade configuration delivers superior overall performance under the present conditions, providing a solid basis for engineering optimization of the mixer geometry.

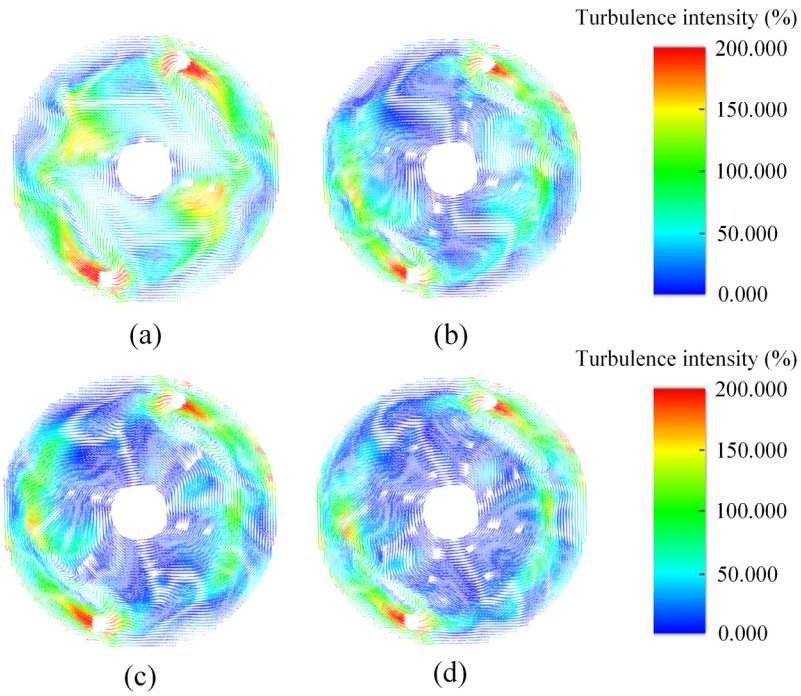


Figure 9. Planar maps of turbulence intensity for different blade counts. (**a**) 2 blades. (**b**) 4 blades. (**c**) 6 blades. (**d**) 8 blades.

A comparative analysis of the time series of turbulence intensity for the blade-number configurations in Figure 10 clearly shows a marked influence of blade count on the evolution of turbulence within the mixer. Over the 2 s simulation window, the four-blade configuration exhibits the most stable turbulence-intensity behavior, with a noticeably smaller fluctuation amplitude than the other cases and a persistently low standard deviation. This stability indicates that the configuration sustains sufficiently turbulent mixing while maintaining a relatively steady flow structure, reflecting a favorable balance between energy input and dissipation. By contrast, the two-blade configuration, limited by weaker agitation, shows overall lower turbulence intensity with pronounced intermittent pulsations. The six- and eight-blade configurations overmix the fluid, complicating the flow structure; their intensity traces display persistent high-frequency oscillations with larger amplitudes, revealing nonsteady energy partitioning and stronger interactions among vortex systems.

In summary, the four-blade configuration demonstrates clear advantages in the time-series behavior of turbulence intensity: the smaller amplitude implies a more stable mixing process and more controllable energy dissipation, which enhances the consistency of mixing efficiency and reduces extra energy losses due to flow oscillations. At the same time, it avoids the under-mixing associated with too few blades and circumvents the risks of excessive energy consumption and equipment vibration associated with too many blades. Therefore, the four-blade design achieves a superior balance across three critical dimensions—mixing efficiency, energy economy, and operational stability—thus offering theoretical and practical guidance for optimizing industrial mixing equipment.

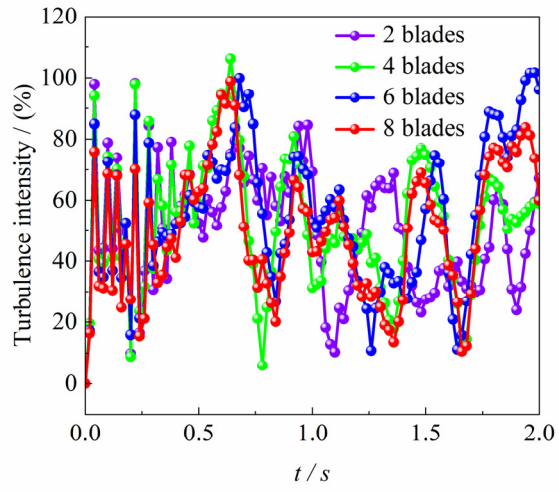


Figure 10. Comparative data of turbulence intensity for different blade counts.

4.2.2. Vorticity-Field Analysis for Different Blade Numbers

Vorticity is a core physical quantity in fluid mechanics for characterizing rotational motion. Analyzing and visualizing the vorticity field enables identification of key flow structures—such as shear layers, separated vortices, and wake regions—whose vorticity concentrations are closely associated with energy losses, vibration noise, and efficiency degradation. Therefore, vorticity serves not only as an essential tool for theoretical analysis of rotational motion but also as a key diagnostic parameter for understanding and optimizing complex internal flows in rotating machinery.

A systematic comparison of the vorticity distributions across blade-number configurations, as shown in Figure 11, clearly reveals a pronounced impact of blade count on the vorticity characteristics inside the mixer. As the blade number increases from 2 to 8, both the spatial complexity and the overall magnitude of the vorticity field rise markedly. Specifically, with two blades, the vorticity distribution is relatively simple: high-vorticity zones remain confined to the blade near field, the number of vortices is limited and their scales are large, indicating comparatively simple rotational dynamics. By contrast, the eight-blade configuration exhibits a highly complex spatial organization: vorticity levels increase substantially and clusters of multiscale, densely packed vortices emerge, greatly strengthening shear and entrainment and thereby improving mixing efficiency.

For intermediate cases, the four- and six-blade configurations display transitional characteristics between these two extremes. Notably, the four-blade design achieves a particularly favorable balance: it generates vortical structures of sufficient strength and number to ensure effective mixing while avoiding the excessive complexity of the vorticity field that can arise with too many blades. This moderate vorticity distribution is of practical engineering significance. It sustains the requisite vortex strength to secure mixing efficiency, while the less convoluted vorticity pattern reduces unnecessary energy dissipation and helps control overall power consumption. At the same time, a more orderly vorticity field promotes flow stability and mitigates the risks of pressure pulsations and equipment vibration caused by intense vortex–vortex interactions. Consequently, the four-blade configuration attains a superior balance among vorticity intensity, energy efficiency, and operational stability, offering important theoretical foundations and practical guidance for optimizing industrial mixing equipment.

According to the vorticity distributions in Figure 12, blade count exerts a pronounced influence on the evolution of the internal vorticity field. As the number of blades increases from 2 to 8, the vorticity levels exhibit a systematic upward trend. Notably, the four- and eight-blade configurations show particularly prominent vorticity peaks, reach-

ing comparatively high levels, which indicates that adding blades effectively strengthens rotational intensity and promotes stronger vortex formation. By contrast, the two-blade case exhibits relatively low vorticity with small fluctuation amplitudes, reflecting weaker rotational motion and limited vortex-generation capacity. The six-blade configuration falls between the others, displaying intermediate vorticity levels and fluctuation characteristics. The increase in blade number enlarges the blade–fluid contact area and modifies shear characteristics, thereby enhancing the conversion efficiency from mechanical input to rotational kinetic energy, which is the principal mechanism underlying the rise in vorticity. However, more blades markedly increase the power requirement and thus energy consumption; additionally, dense blade arrangements may induce more complex flow-interference phenomena, intensifying pressure pulsations and potentially compromising structural integrity and operational stability. Therefore, the choice of blade count in mixer design and optimization should comprehensively balance mixing efficiency, energy economy, and equipment reliability.

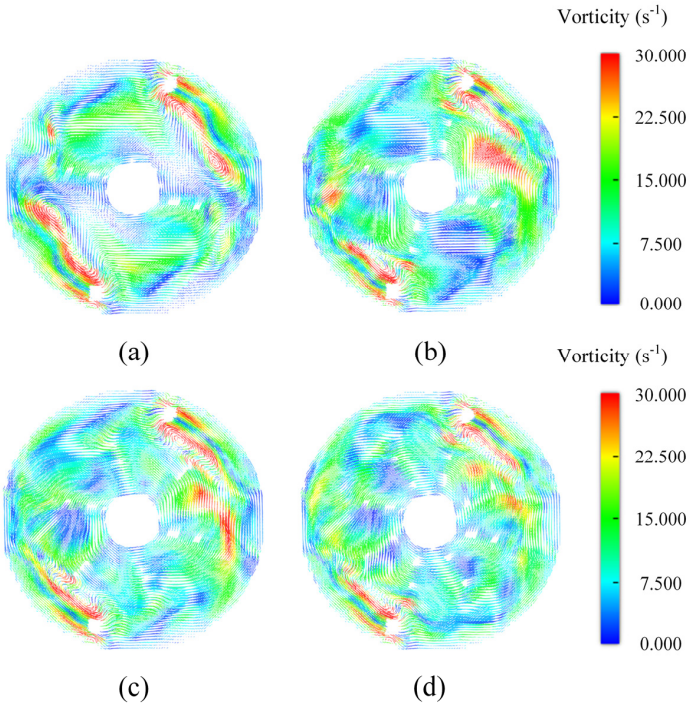


Figure 11. Planar vorticity maps for different blade counts. (**a**) 2 blades. (**b**) 4 blades. (**c**) 6 blades. (**d**) 8 blades.

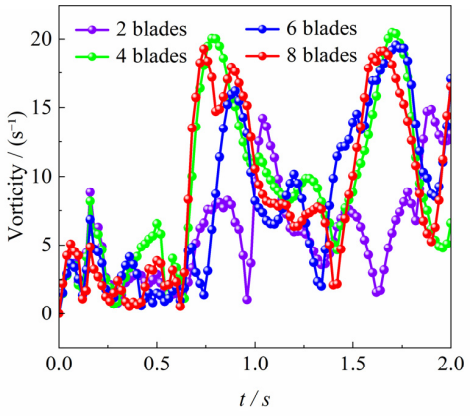


Figure 12. Comparative vorticity data for different blade counts.

4.3. Analysis of Flow-Field Data at Monitoring Points for Different Blade Numbers

To investigate the flow-field dynamics and spatial distribution in greater depth, four key monitoring points are systematically arranged within the mixing chamber to acquire time histories of turbulence intensity and vorticity under different blade-number configurations, as shown in Figure 13. Placement follows hydrodynamic diagnostic principles: Points 1 and 2 are located beneath the main-shaft impeller in the core flow region to capture features of the primary flow dominated by main-shaft rotation, whereas Points 3 and 4 are symmetrically positioned beneath the side-shaft impellers to sample the secondary flow and the main–side shaft interaction zone. This spatially discretized monitoring strategy covers representative locations of distinct functional regions and, through comparative analysis, reveals the spatial heterogeneity of the flow structure. Time-series and statistical analyses of turbulence intensity and vorticity at each point enable quantitative assessment of how blade number modulates both local and global flow structures, thereby supplying robust evidence for constructing correlation models between blade parameters and mixing performance.

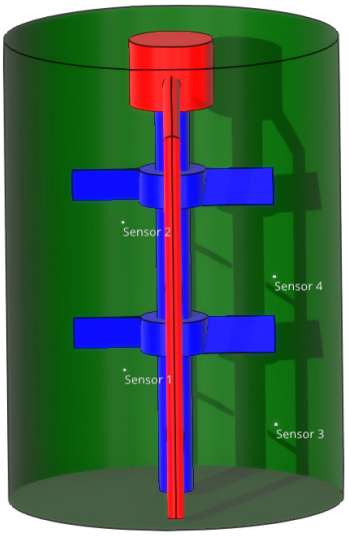


Figure 13. Layout of monitoring points.

4.3.1. Turbulence-Intensity Analysis at Four Monitoring Points for Different Blade Numbers

Figure 14 presents a comparative plot of turbulence intensity at the four monitoring points for different blade numbers. A pronounced spatial nonuniformity of the internal turbulence field is clearly observed. Turbulence intensity at Points 2 and 3 is systematically higher—in both peak magnitude and fluctuation severity—than at Points 1 and 4. This spatial pattern indicates that strong shear layers and periodic vortex shedding induced by impeller rotation primarily occur near Points 2 and 3. These zones constitute the core regions of turbulence production and dissipation, playing a decisive role in fragmenting fluid microelements and promoting mixing.

A systematic comparison of turbulence-intensity evolution across blade-number configurations further elucidates the regulatory mechanism by which blade count shapes the flow structure. With two blades, the turbulence intensity at Points 1 and 2 beneath the main shaft exhibits very high peaks and sharp intermittency, indicating pronounced localization of shear stress. Although such intense turbulence can boost instantaneous mixing, its strong unsteadiness tends to cause local nonuniformity. As the blade number increases to six and eight, the flow characteristics change markedly. The turbulence-intensity traces at all points become smoother; notably, in the side-shaft regions, conspicuous peaks almost vanish,

suggesting a near-laminar regime in which instability risks associated with excessive local turbulence are effectively mitigated. This improvement in flow uniformity helps reduce local energy dissipation and the likelihood of hot-spot formation.

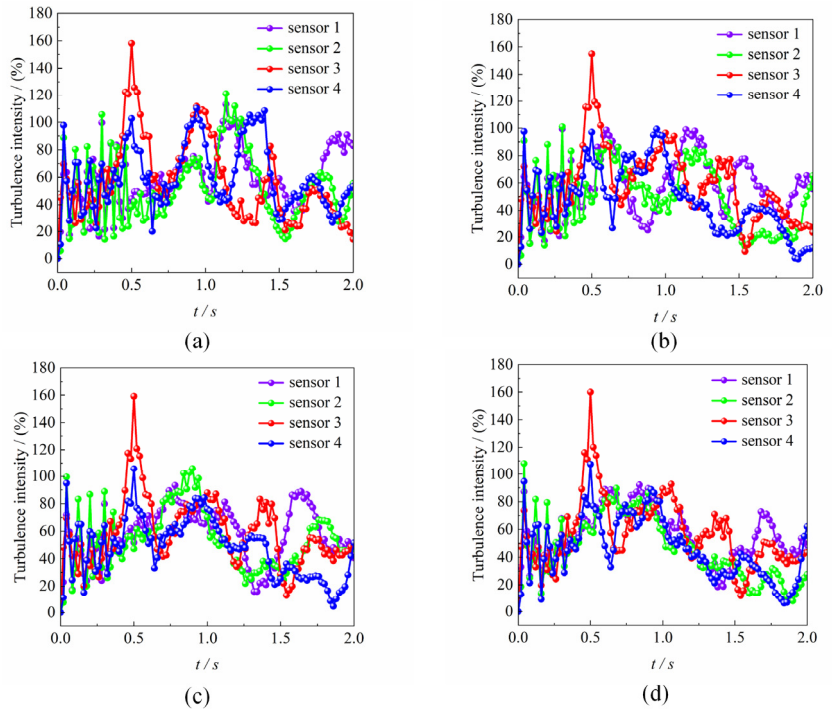


Figure 14. Comparison of turbulence intensity at four monitoring points for different blade counts: (**a**) 2 blades. (**b**) 4 blades. (**c**) 6 blades. (**d**) 8 blades.

Of particular interest are the flow features under the four-blade configuration. This configuration generates a highly unsteady turbulent environment across the vessel: at Monitoring Points 1 and 2 beneath the main-shaft impeller, the turbulence intensity exhibits regular, periodic, and intense fluctuations in the range of 20–140, directly corresponding to strong shear and vortex shedding induced as the blades periodically sweep the monitoring zones. In the side-shaft region, Points 3 and 4 display more complex fluctuation patterns; notably, Point 3 reaches an instantaneous peak of 160 around t = 0.5 s, markedly exceeding the other points, indicating a stronger and more direct disturbance from the side-shaft impeller on the underlying flow and the possible formation of a local high-dissipation zone.

A comprehensive analysis indicates that the four-blade twin-shaft mixer establishes a well-developed yet relatively coordinated turbulent environment throughout the tank, which is highly favorable for simultaneously sustaining macroscopic mixing efficiency and microscale mass-transfer rates. By maintaining sufficient turbulence intensity near the main shaft to promote mixing while allowing moderate fluctuations near the side shafts to control energy usage, it achieves an optimal balance between mixing performance and energy efficiency, thereby offering important theoretical guidance for the optimization of industrial mixing devices.

4.3.2. Vorticity-Field Analysis at Four Monitoring Points for Different Blade Numbers

Figure 15 presents the vorticity fields at four monitoring points for different blade numbers, systematically revealing the profound impact of blade count on the structure and evolution dynamics of the vortex field inside the mixer. Across all cases, a clear common pattern emerges: the mean vorticity and fluctuation amplitude at Points 3 and 4—located beneath the side-shaft impellers—are markedly higher than those at Points 1 and 2 beneath the main-shaft impeller. This spatial distribution indicates that, in twin-shaft systems, the

dominant regions of vortex generation and the core zones of strong shear are concentrated near the rapidly rotating side-shaft impellers. Tip vortices produced and shed periodically by the side-shaft impellers serve as the principal carriers of energy transport and material dispersion in the flow, forming the physical basis for efficient mixing; by contrast, the flow beneath the main-shaft impeller exhibits comparatively milder vorticity features.

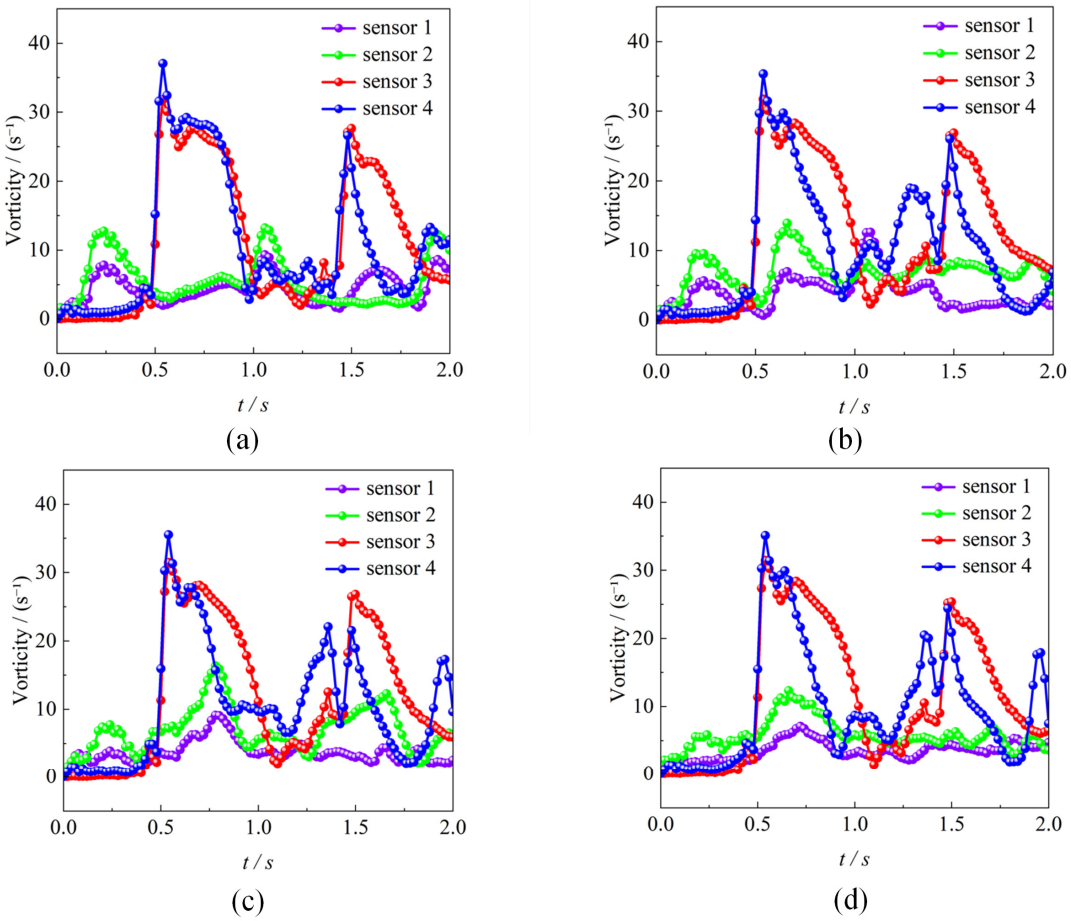


Figure 15. Comparative vorticity fields at four monitoring points for different blade counts: (**a**) 2 blades. (**b**) 4 blades. (**c**) 6 blades. (**d**) 8 blades.

A comparative assessment across configurations shows that blade number decisively regulates vortex intensity, occurrence frequency, and evolution patterns. For the four-blade configuration, instantaneous vorticity peaks at Points 3 and 4 reach approximately 35 s^{-1}, the highest among all cases. This indicates that the configuration induces the most intense concentrated vortices, thereby providing optimal instantaneous shear—highly advantageous for dispersion processes requiring efficient breakup of particles or droplets. With only two blades, intermittent vorticity peaks are observed but occur at a much lower frequency, leading to poor temporal continuity of mixing. Conversely, for six and eight blades, high-frequency pulsations become more evident, yet the peak vorticity levels decrease systematically. This behavior is attributable to reduced blade spacing, which limits the full development and roll-up of individual vortices; neighboring vortical structures then interfere and break up prematurely, ultimately diminishing the effective shear-energy level of the overall vortex field. Therefore, the four-blade mixer achieves an optimal balance between vortex intensity and evolution characteristics; its design excites strong, well-periodic concentrated vortices in the side-shaft region, furnishing flow conditions that are optimal for efficient dispersion and mixing. Therefore, the four-blade mixer achieves an optimal balance between vortex intensity and evolution characteristics; its design

excites strong, well-periodic concentrated vortices in the side-shaft region, furnishing flow conditions that are optimal for efficient dispersion and mixing.

5. Conclusions

This study develops a high-fidelity numerical framework for twin-shaft mixers by coupling LBM–LES with a moving-boundary treatment and a D3Q27 velocity set, thereby resolving three-dimensional, strongly unsteady vortex evolution and turbulent pulsations without resorting to overset meshes. A resolution-independence study establishes an accuracy–cost compromise, after which the framework systematically elucidates flow–mixing coupled dynamics for different blade numbers within a fixed twin-shaft arrangement, enabling interpretable links among structure, operating condition, flow field, and performance. Although the present geometry keeps the relative shaft positions and diameters constant, alternative shaft configurations represent an important topic for future investigation.

1. The proposed LBM–LES coupling with moving boundaries eliminates the need for remeshing and mitigates interpolation errors in complex geometries, markedly improving the resolution of high-Re, strong-shear unsteady processes. The multi-relaxation-time (MRT) collision operator and subgrid-scale LES modeling jointly enhance numerical robustness, enabling stable simulations at Reynolds numbers exceeding 10^5. The present single-phase cases confirm stability without artificial damping, and the same framework has been successfully extended in prior LBM–LES–DEM and multiphase LBM studies to strongly sheared particulate and gas–liquid flows. Nevertheless, fully resolved multiphase mixing with interfacial deformation lies beyond the current scope and will require future coupling with explicit interface-capturing schemes. Cross-resolution comparisons and stability assessments confirm convergence and consistency of macroscopic quantities (pressure, velocity, turbulent kinetic energy) under the chosen accuracy–cost balance. In addition, the momentum-exchange method at boundaries connects simulated forces and power directly to equipment selection and energy-efficiency evaluation.
2. Mechanistically, the results delineate a tiered sequence from tip shear, through localized vortices, to energy backscatter. Peaks of turbulent kinetic energy and vorticity remain anchored near blade tips and beneath side-shaft impellers, exhibiting periodic pulsations and spatial migration. By contrast, the region beneath the main shaft is comparatively quiescent and helps sustain global recirculation and energy redistribution. Multi-point monitoring indicates that the zones beneath the side shafts constitute principal channels for turbulence production and dissipation, acting as bottlenecks or valves that regulate microscale entrainment and macroscopic circulation closure.
3. Regarding parameter effects, blade-number-dependent differences follow clear trends. With two blades, large-amplitude pulsations and localized shear concentrations arise beneath the main shaft, yielding strong yet nonuniform mixing. With six and eight blades, inter-blade interference limits the full development of individual vortices, lowering peak vorticity while increasing the risk of higher power consumption. The four-blade configuration achieves a balanced compromise among vortex intensity, turbulent-energy coverage, and controllable pulsations, thereby supporting efficient dispersion together with stable recirculation.

Author Contributions: W.Z.: writing—review and editing, writing—original draft, resources, project administration, methodology, investigation, data curation, conceptualization. L.L.: validation, supervision, resources, investigation. J.Y.: data curation, conceptualization. G.Z.: visualization, validation, methodology, formal analysis, supervision, funding acquisition, writing—review and editing. All authors have read and agreed to the published version of the manuscript.

Funding: This research was supported by the Zhejiang Provincial Natural Science Foundation of China under Grant No. LGF22F030014.

Data Availability Statement: Data will be made available on request.

Conflicts of Interest: The authors declare no conflicts of interest.

References

1. Lv, X.; Bai, B.; Zhao, Y.; Liu, Y.; Ma, Q.; Wang, C.; Zhou, S.; Song, S.; Shi, B. Study on rheological properties of natural gas hydrate slurry. *Chem. Eng. Res. Des.* **2022**, *188*, 779–789. [CrossRef]
2. Sokhandan, F.; Homayoonfal, M.; Hajheidari, M. Sodium alginate coating: A strategy to fabricate a membrane surface resistant against sodium alginate fouling. *Chem. Eng. Res. Des.* **2021**, *176*, 202–217. [CrossRef]
3. Li, W.; Yang, Q.; Yang, Y.; Ji, L.; Shi, W.; Agarwal, R. Optimization of pump transient energy characteristics based on response surface optimization model and computational fluid dynamics. *Appl. Energy* **2024**, *362*, 123038. [CrossRef]
4. Yan, Q.; Li, L.; Tan, Y.F. Energy transfer characteristics of surface vortex heat flow under non-isothermal conditions based on the lattice Boltzmann method. *Processes*, 2026; *in press*.
5. Zheng, G.A.; Weng, X.X.; Wang, T.; Xu, P.; Xu, W.X.; Li, L.; Xu, X.F.; Tan, D.P. Piezoelectric ultrasonic coupling-based polishing of micro-tapered holes with abrasive flow. *J. Zhejiang Univ.-Sci. A*, 2025, *in press*. [CrossRef]
6. Sun, Z.; Yao, Q.; Jin, H.; Xu, Y.; Hang, W.; Chen, H.; Li, K.; Shi, L.; Gu, J.; Zhang, Q.; et al. A novel in-situ sensor calibration method for building thermal systems based on virtual samples and autoencoder. *Energy* **2024**, *297*, 131314. [CrossRef]
7. Sun, Z.; Yao, Q.; Shi, L.; Jin, H.; Xu, Y.; Yang, P.; Xiao, H.; Chen, D.; Zhao, P.; Shen, X. Virtual sample diffusion generation method guided by large language model-generated knowledge for enhancing information completeness and zero-shot fault diagnosis in building thermal systems. *J. Zhejiang Univ.-Sci. A (Appl. Phys. Eng.)* **2025**, *26*, 895–916. [CrossRef]
8. Wang, T.; Li, L.; Zhang, Y.; Li, J.C.; Wan, Q.J.; Tan, D.P. Analytical treatment and experimental investigation of forced displacement responses of cracked fluid-filled thin cylindrical shells. *Thin Wall Struct.* 2025, *in press*.
9. Hwang, M.-S.; Kim, H.-R.; Kim, J.; Yang, B.-J.; Kivshar, Y.; Park, H.-G. Vortex nanolaser based on a photonic disclination cavity. *Nat. Photonics* **2024**, *18*, 286–293. [CrossRef]
10. Hou, J.; Liu, Y. Evolution of unsteady vortex structures in the tip region of an axial compressor rotor. *Phys. Fluids* **2023**, *35*, 045107. [CrossRef]
11. Gu, Y.; Ma, L.; Yu, S.; Yan, M.; Wu, D.; Mou, J. Surface cavitation flow characterization of jet hydrofoils based on vortex identification method. *Phys. Fluids* **2023**, *35*, 012112. [CrossRef]
12. Fu, M.; Han, G.; Lu, X.; Sun, W.; Sommeria, J.; Stegner, A.; Caldeira, R.M.; Dong, C. Analysis of vortex merging from a rotating tank laboratory experiment. *Prog. Oceanogr.* **2024**, *222*, 103227. [CrossRef]
13. Wang, S.; Xiong, X.; Liu, P.; Zhang, Q.; Zhang, Q.; Tao, C.; Wang, Y.; Liu, Z. CFD simulation of hydrodynamics and mixing performance in dual shaft eccentric mixers. *Chin. J. Chem. Eng.* **2023**, *62*, 297–309. [CrossRef]
14. Li, W.; Ji, L.; Shi, W.; Zhou, L.; Agarwal, R.; Mahmouda, E. Numerical investigation of internal flow characteristics in a mixed-flow pump with eccentric impeller. *J. Braz. Soc. Mech. Sci. Eng.* **2020**, *42*, 458. [CrossRef]
15. Talhaoui, A.; Draoui, B.; Youcefi, A. Effect of Geometry Design on Mixing Performance of Newtonian Fluids using Helical Overlapped Mixer Elements in Kenics Static Mixer. *J. Appl. Fluid Mech.* **2021**, *14*, 1643–1656. [CrossRef]
16. Woziwodzki, S.; Jędrzejczak, Ł. Effect of eccentricity on laminar mixing in vessel stirred by double turbine impellers. *Chem. Eng. Res. Des.* **2011**, *89*, 2268–2278. [CrossRef]
17. Raval, S.; Holloway, A.G.L. Experimental study of dual-impeller string vibration in a baffled mixing vessel. *Int. J. Press. Vessel. Pip.* **2018**, *165*, 306–321. [CrossRef]
18. Bobba, D.; Tabei, S.A.; Cherukuri, H.P.; Pando, M.A. DEM simulation of particle segregation in filling of vibratory dies. *Adv. Powder Technol.* **2020**, *31*, 3474–3484. [CrossRef]
19. Trad, Z.; Fontaine, J.-P.; Larroche, C.; Vial, C. Experimental and numerical investigation of hydrodynamics and mixing in a dual-impeller mechanically-stirred digester. *Chem. Eng. J.* **2017**, *329*, 142–155. [CrossRef]
20. Emmerink, J.; Hadi, A.; Jovanova, J.; Cleven, C.; Schott, D.L. Parametric analysis of a double shaft, batch-type paddle mixer using the discrete element method (DEM). *Processes* **2023**, *11*, 738. [CrossRef]

21. GYang, G.; Jing, L.; Kwok, C.; Sobral, Y. A comprehensive parametric study of LBM-DEM for immersed granular flows. *Comput. Geotech.* **2019**, *114*, 103100. [CrossRef]
22. Reinecke, S.; Blahout, S.; Zhang, Z.; Rosemann, T.; Hussong, J.; Kruggel-Emden, H. Effects of particle size, particle density, and Reynolds number on equilibrium streaks forming in a square wave serpentine microchannel: A DEM-LBM simulation study including experimental validation of the numerical framework. *Powder Technol.* **2023**, *427*, 118688. [CrossRef]
23. Xu, W.; Xu, P.; Yang, Y.; Tan, D.; Li, L. Utilization and advancement of laser ultrasound testing in assessment of aerospace composite characteristics: A review. *Chin. J. Aeronaut.* **2025**, *38*, 103789. [CrossRef]
24. Cui, X.; Wang, Z.; Yao, X.; Liu, M.; Yu, F. A coupled two-relaxation-time lattice Boltzmann-volume penalization method for flows past obstacles. *Math. Comput. Simul.* **2022**, *198*, 85–105. [CrossRef]
25. Guo, Z.; Zheng, C. Analysis of lattice Boltzmann equation for microscale gas flows: Relaxation times, boundary conditions and the Knudsen layer. *Int. J. Comput. Fluid Dynam.* **2008**, *22*, 465–473. [CrossRef]
26. Liu, L.; Meng, Z.; Zhang, Y.; Sun, Y. Simulation of High-Viscosity Generalized Newtonian Fluid Flows in the Mixing Section of a Screw Extruder Using the Lattice Boltzmann Model. *ACS Omega* **2023**, *8*, 47991–48018. [CrossRef]
27. Chen, H.; Liu, W.; Li, S. A fully-resolved LBM-LES-DEM numerical scheme for adhesive and cohesive particle-laden turbulent flows in three dimensions. *Powder Technol.* **2024**, *440*, 119800. [CrossRef]
28. Chen, H.; Liu, W.; Chen, Z.; Zheng, Z. A numerical study on the sedimentation of adhesive particles in viscous fluids using LBM-LES-DEM. *Powder Technol.* **2021**, *391*, 467–478. [CrossRef]
29. Noble, D.R.; Torczynski, J.R. A lattice-Boltzmann method for partially saturated computational cells. *Int. J. Mod. Phys. C* **1998**, *9*, 1189–1201. [CrossRef]
30. Fu, S.; Wang, L. GPU-based unresolved LBM-DEM for fast simulation of gas–solid flows. *Chem. Eng. J.* **2023**, *465*, 142898. [CrossRef]
31. Chen, W.; Song, Z.; Quan, D.; He, Y. Regulating Melting Process in the Energy Storage of Solid-Liquid PCM based on Double MRT-LBM Simulation. *J. Therm. Sci.* **2024**, *33*, 1688–1700. [CrossRef]
32. Li, Q.; Tang, R.; Wang, S.; Zou, Z. A coupled LES-LBM-IMB-DEM modeling for evaluating pressure drop of a heterogeneous alternating-layer packed bed. *Chem. Eng. J.* **2022**, *433*, 133529. [CrossRef]
33. Oh, G.; Yang, M.; Choi, J.-I. Large-eddy simulation-based wind and thermal comfort assessment in urban environments. *J. Wind Eng. Ind. Aerodyn.* **2024**, *246*, 105682. [CrossRef]
34. Zhou, D.; Bae, H.J. Sensitivity analysis of wall-modeled large-eddy simulation for separated turbulent flow. *J. Comput. Phys.* **2024**, *506*, 112948. [CrossRef]
35. Tan, Y.; Li, Q.; Li, L.; Tan, D. Investigating the Regulatory Mechanism of the Baffle Geometric Parameters on the Lubrication Transmission of High-Speed Gears. *Appl. Sci.* **2025**, *15*, 11080. [CrossRef]
36. Zhao, W. A Study on the Influence Mechanism of the Oil Injection Distance on the Oil Film Distribution Characteristics of the Gear Meshing Zone. *Machines* **2025**, *13*, 606. [CrossRef]
37. Lin, Q.; Li, Q.; Xu, P.; Zheng, R.; Bao, J.; Li, L.; Tan, D. Transport Mechanism and Optimization Design of LBM-LES Coupling-Based Two-Phase Flow in Static Mixers. *Processes* **2025**, *13*, 1666. [CrossRef]
38. Wang, Y.; Luo, Z.; Zhou, Y.; Peng, W. Large eddy simulation of pulsating film cooling on turbine vane. *Aerosp. Sci. Technol.* **2024**, *148*, 109103. [CrossRef]
39. Saavedra, L.P.; Radburn, C.E.N.; Collard-Daigneault, A.; Blais, B. An implicit large-eddy simulation perspective on the flow over periodic hills. *Comput. Fluids* **2024**, *283*, 106390. [CrossRef]
40. Yamamoto, T.; Murata, A.; Inokuma, K.; Iwamoto, K. Heat transfer augmentation due to flow pulsation in a channel with teardrop-shaped dimples investigated by large eddy simulation. *Int. J. Heat Fluid Flow* **2024**, *110*, 109579. [CrossRef]
41. Tao, Z.; Yu, B.; Liu, X.; Song, L.; Li, J. Large eddy simulation on unsteady flow and heat transfer behaviors of double swirl cooling configuration. *Int. Commun. Heat Mass Transf.* **2024**, *157*, 107752. [CrossRef]
42. Zhang, S.; Law, A.W.-K. Performance of Reynolds averaged Navier–Stokes and large eddy simulation models in simulating flows in a crossflow ultraviolet reactor: An experimental evaluation. *Water* **2024**, *16*, 271. [CrossRef]
43. Li, Y.; Yan, L.; He, X. Large eddy simulation study of 3D wind field in a complex mountainous area under different boundary conditions. *J. Zhejiang Univ.-Sci. A* **2024**, *25*, 541–556. [CrossRef]
44. Yin, Z.; Ni, Y.; Li, L.; Wang, T.; Wu, J.; Li, Z.; Tan, D. Numerical modeling and experimental investigation of a two-phase sink vortex and its fluid-solid vibration characteristics. *J. Zhejiang Univ.-Sci. A* **2024**, *25*, 47–62. [CrossRef]
45. Amatriain, A.; Gargiulo, C.; Rubio, G. Generalized wall-modeled large eddy simulation model for industrial applications. *Phys. Fluids* **2024**, *36*, 015141. [CrossRef]
46. Zhou, T.; Li, F. Large eddy simulation of non-premixed flame behavior and NOx emission characteristics in a staged combustor with multi-swirling flows. *Appl. Therm. Eng.* **2024**, *246*, 123020. [CrossRef]
47. Smagorinsky, J. General circulation experiments with the primitive equations: I. The basic experiment. *Mon. Weather Rev.* **1963**, *91*, 99–164. [CrossRef]

48. Eichler, P.; Fučík, R.; Strachota, P. Investigation of mesoscopic boundary conditions for lattice Boltzmann method in laminar flow problems. *Comput. Math. Appl.* **2024**, *173*, 87–101. [CrossRef]
49. Li, L.; Xu, P.; Li, Q.; Yin, Z.; Zheng, R.; Wu, J.; Bao, J.; Bai, W.; Qi, H.; Tan, D. Multi-field coupling particle flow dynamic behaviors of the microreactor and ultrasonic control method. *Powder Technol.* **2025**, *454*, 120731. [CrossRef]
50. Kang, J.; Wu, D. A structurally compatible forcing scheme for three-dimensional cumulant lattice Boltzmann method. *Comput. Fluids* **2025**, *300*, 106762. [CrossRef]
51. Li, L.; Xu, P.; Li, Q.; Zheng, R.; Xu, X.; Wu, J.; He, B.; Bao, J.; Tan, D. A coupled LBM-LES-DEM particle flow modeling for microfluidic chip and ultrasonic-based particle aggregation control method. *Appl. Math. Model.* **2025**, *143*, 116025. [CrossRef]
52. Wang, C.; Li, Z.; Xu, P.; Hou, Y.; Tan, D.; Li, L. Collision modeling approach and transient response mechanism of ring-ribbed cylindric shells for underwater vehicles. *Appl. Math. Model.* **2025**, *141*, 115923. [CrossRef]
53. Yinglei, G.; Shuai, W. Influence of porous structure on bubble dynamics and boiling heat transfer characteristics on the vertically heating surface via LBM approach. *Int. Commun. Heat Mass Transf.* **2025**, *162*, 108592. [CrossRef]
54. Liu, C.; Sun, C.; Dai, L.; Wang, G.; Shao, H.; Li, W.; Long, W. Integrating Laboratory-Measured Contact Angles into Time-Dependent Wettability-Adjusted LBM Simulations for Oil–Water Relative Permeability. *Energies* **2025**, *18*, 2404. [CrossRef]
55. Kang, Q.; He, D.; Zhao, N.; Feng, X.; Wang, J. Hydrodynamics in unbaffled liquid-solid stirred tanks with free surface studied by DEM-VOF method. *Chem. Eng. J.* **2020**, *386*, 122846. [CrossRef]
56. Li, L.; Xu, P.; Xu, W.X.; Lu, B.; Wang, C.Y.; Tan, D.P. Multi-field coupling vibration patterns of the multiphase sink vortex and distortion recognition method. *Mech. Syst. Signal Process.* **2024**, *219*, 111624. [CrossRef]
57. Cao, X.; Chen, Y.P. Design and numerical analysis of serpentine microchannel integrated with inner-wall ridges for enhanced droplet mixing. *Sci. China Technol. Sci.* **2023**, *66*, 560–573. [CrossRef]
58. Li, L.; Lu, B.; Xu, W.; Wang, C.Y.; Wu, J.F.; Tan, D.P. Dynamic behaviors of multiphase vortex-induced vibration for hydropower energy conversion. *Energy* **2024**, *308*, 132897. [CrossRef]
59. Li, L.; Xu, P.; Li, Q.; Zheng, R.; Wu, N.; Bao, J.; Xu, W.; Ma, Q.; Yin, Z. Fluid-induced energy transfer and vibration modes of multiphase mixing in static mixers across flow regime transitions. *Chem. Eng. J.* 2026; *in press*.
60. Montante, G.; Paglianti, A.; Magelli, F. Analysis of dilute solid–liquid suspensions in turbulent stirred tanks. *Chem. Eng. Res. Des.* **2012**, *90*, 1448–1456. [CrossRef]

Disclaimer/Publisher's Note: The statements, opinions and data contained in all publications are solely those of the individual author(s) and contributor(s) and not of MDPI and/or the editor(s). MDPI and/or the editor(s) disclaim responsibility for any injury to people or property resulting from any ideas, methods, instructions or products referred to in the content.